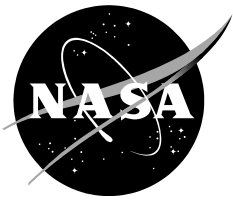# Full-Field Reconstruction of Structural Deformations and Loads from Measured Strain Data on a Wing Test Article using the Inverse Finite Element Method

Eric J. Miller, and Russel Manalo
Armstrong Flight Research Center, Edwards, California

Alexander Tessler
Langley Research Center, Hampton, Virginia

NASA STI Program ... in Profile

Since its founding, NASA has been dedicated to the advancement of aeronautics and space science. The NASA scientific and technical information (STI) program plays a key part in helping NASA maintain this important role.

The NASA STI program operates under the auspices of the Agency Chief Information Officer. It collects, organizes, provides for archiving, and disseminates NASA's STI. The NASA STI program provides access to the NTRS Registered and its public interface, the NASA Technical Reports Server, thus providing one of the largest collections of aeronautical and space science STI in the world. Results are published in both non-NASA channels and by NASA in the NASA STI Report Series, which includes the following report types:
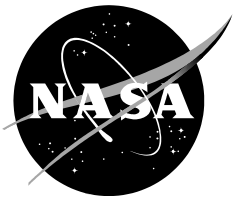
- TECHNICAL PUBLICATION. Reports of completed research or a major significant phase of research that present the results of NASA Programs and include extensive data or theoretical analysis. Includes compilations of significant scientific and technical data and information deemed to be of continuing reference value. NASA counterpart of peer-reviewed formal professional papers but has less stringent limitations on manuscript length and extent of graphic presentations.

- TECHNICAL MEMORANDUM. Scientific and technical findings that are preliminary or of specialized interest, e.g., quick release reports, working papers, and bibliographies that contain minimal annotation. Does not contain extensive analysis.

- CONTRACTOR REPORT. Scientific and technical findings by NASA-sponsored contractors and grantees.

- CONFERENCE PUBLICATION. Collected papers from scientific and technical conferences, symposia, seminars, or other meetings sponsored or co-sponsored by NASA.

- SPECIAL PUBLICATION. Scientific, technical, or historical information from NASA programs, projects, and missions, often concerned with subjects having substantial public interest.

- TECHNICAL TRANSLATION. English-language translations of foreign scientific and technical material pertinent to NASA's mission.

Specialized services also include organizing and publishing research results, distributing specialized research announcements and feeds, providing information desk and personal search support, and enabling data exchange services.

For more information about the NASA STI program, see the following:

- Access the NASA STI program home page at http://www.sti.nasa.gov

- E-mail your question to help@sti.nasa.gov

- Phone the NASA STI Information Desk at 757-864-9658

- Write to:
  NASA STI Information Desk
  Mail Stop 148
  NASA Langley Research Center
  Hampton, VA 23681-2199

Full-Field Reconstruction of Structural Deformations and Loads from Measured Strain Data on a Wing Test Article using the Inverse Finite Element Method

Eric J. Miller, and Russel Manalo
Armstrong Flight Research Center, Edwards, California

Alexander Tessler
Langley Research Center, Hampton, Virginia

November 2016

This report is available in electronic form at

http://www.ntrs.nasa.gov

Abstract

A study was undertaken to investigate the measurement of wing deformation and internal loads using measured strain data. Future aerospace vehicle research depends on the ability to accurately measure the deformation and internal loads during ground testing and in flight. The approach uses the inverse Finite Element Method (iFEM). The iFEM is a robust, computationally efficient method that is well suited for real-time measurement of real-time structural deformation and loads. The method has been validated in previous work, but has yet to be applied to a large-scale test article. This work is in preparation for an upcoming loads test of a half-span test wing in the Flight Loads Laboratory at the National Aeronautics and Space Administration Armstrong Flight Research Center (Edwards, California). The method has been implemented into an efficient MATLAB® (The MathWorks, Inc., Natick, Massachusetts) code for testing different sensor configurations. This report discusses formulation and implementation along with the preliminary results from a representative aerospace structure. The end goal is to investigate the modeling and sensor placement approach so that the best practices can be applied to future aerospace projects.

Nomenclature

AFRC	Armstrong Flight Research Center
CAD	computer-aided design
DOF	degrees of freedom
FEM	finite element method
FOSS	fiber optic strain sensing
iFEM	inverse Finite Element Method
MPD	mean percent difference
NASA	National Aeronautics and Space Administration
PD	percent difference
c_i	local chord length
δ	nodal displacement
θ	wing twist angle
3-D	three-dimensional

Introduction

The National Aeronautics and Space Administration (NASA) Armstrong Flight Research Center (AFRC) (Edwards, California) has an extensive history of testing one-of-a-kind flight research vehicles. New and innovative aerospace structures are being developed to operate differently than the conventional aluminum and fiber composite structures that have been built over the past 50 years. This new class of aerospace vehicles will push aspect ratios beyond current industry limits and allow structures to deform to create improved aerodynamic surfaces. These structures will require new methods of in-flight health monitoring for enhancing flight safety. Research in the areas of sensor technology and structural algorithms is an important aspect for enabling real-time deformation and health-monitoring applications, structural control feedback, and lightweight structures. The current goals align with noise reduction, weight reduction, and optimizing efficiency.

To date, a large body of work has been carried out in the areas of structural sensor technology and structural monitoring algorithms. The sensor technology most commonly used to monitor structures includes conventional metallic foil strain gages and fiber optic strain sensing (FOSS) systems. Conventional metallic foil strain gages have been used in the industry for many years and form the backbone of structural monitoring capabilities. Fiber optic strain sensing is a somewhat newer capability that has advanced greatly in the past decade and allows the ability to monitor multiple strain sensors by a single optical fiber. Strains

measured every one-half-inch along a 40-ft-long single optical fiber at rates of approximately 40Hz has become commonplace in the field of fiber optic sensors. The advancement of these systems has given researchers the capability of gathering large amounts of structural data. The question that arises is how an engineer makes use of all of these data to enable higher performing structures.

The current investigation concentrates on a triangular element formulation so that a foundation may be developed for studying adaptive structures and future aerospace vehicle applications. The motivation for this work has come from the requirement to monitor in-flight deformation and loads from aerospace structures currently being tested at NASA AFRC. Results from numerical examples are given. Numerical examples highlight the process of taking experimental strains and calculating the nodal displacements. The nodal displacements are then used to calculate the internal loads in the structure. An example is shown to highlight the applicability of this method to aerospace structures.

The purpose of this report is to provide a status of the work to date regarding the implementation of the inverse Finite Element Method (iFEM) into the MATLAB® (The MathWorks, Inc., Natick, Massachusetts) code for calculating structural deformation and internal loading of aerospace structures. The full process of instrumentation to finite element model generation is presented along with lessons learned for future assessments.

Previous Work

This report focuses on one of many methods that have been developed for structural monitoring algorithms. Other methods, such as the Displacement Transfer Function Method, developed in-house at NASA AFRC take the classical beam equations and use piecewise polynomials to approximate beam curvature. The Displacement Transfer Function Method has been shown to work well on cantilevered structures and has been applied to experimental tests conducted in the Flight Loads Laboratory at NASA AFRC (ref. 1). In addition to that method, Dr. Chan-gi Pak of AFRC uses a similar method of using beam equations to calculate the structural deformed shape under load to calculate aerodynamic forces (ref. 2).

These two beam methods cannot generate a full three-dimensional (3-D) deformed shape and full-field strain map for structures that are more complicated than what can be easily represented by a characteristic beam. Complex structures that cannot be represented by simple beam formulations require the use of inverse methods. Inverse problems are ill-posed from the standpoint of not being able to satisfy conditions of existence, uniqueness, and stability. In terms of uniqueness, a structure may contain a nearly infinite number of strain sensors. Stability is affected by the influence of noise on each sensor; a small disturbance in the strain can induce large changes in the displacement solution.

Tikhonov and Arsenin (ref. 3) developed a method for approximating solutions that are stable under small variations in the measured data. Most inverse methods in use today can be traced back to Tikhonov's regularization method. Multiple inverse methods can be found in the literature (refs. 4-7) but few are sufficient to deal with the reconstruction of three-dimensional deformation of complex structures. In addition, most methods are not formulated for dealing with the required magnitude of computations required for supporting shell and plate formulations.

A few inverse methods using least-squares approaches should be noted. An approach by Bogert et al. (ref. 8) applied a least-squares approach to develop strain-to-displacement transformations using a modal transformation method. The method is computationally intensive because of the need for a large number of vibration modes. In another approach, Jones et al. (ref. 9) calculated the deformation in a cantilever plate using axial strains that were fitted with a cubic polynomial. Lastly, Shkarayev et al. (refs. 10, 11) implemented a two-step procedure. The first step requires the analysis of a structural finite element model. A least-squares approach is then applied in the second step to calculate the displacements. This method requires first calculating the applied loading.

All of these methods are insufficient for efficient real-time calculation of complex structural deformed shapes. The inadequacy of each method may be due to the formulation being insufficient to characterize the complex deformation, or to its computationally intensive nature. None of these methods are adequate

from a real-time structural-health-monitoring standpoint. The capable method must maintain real-time computational efficiency, robustness, and the ability to model complex structural geometries.

The iFEM discussed in this report was developed by Tessler and Spangler over the last 15 years at the NASA Langley Research Center (Hampton Virginia) (LARC) (refs. 12-15). It was developed using a three-node shell element formulated using a weighted least-squares variational principle. Most of the work using this method has been performed at NASA LARC. The method has been shown to work on simple test articles, but has yet to be applied to large aerospace structures (ref. 16). Related work by Marco Gherlone and his colleagues at the Politecnico di Torino in Torino, Italy took the iFEM and applied it to frame elements of circular cross-section using a minimal number of strain sensors (ref. 17). Recently, Kefal et al. (refs. 18-20) used the original Tessler-Spangler iFEM formulation and derived a four-node quadrilateral inverse shell element. This new element was applied to marine applications.

The iFEM is referred to as a structural monitoring algorithm throughout this report because the framework of the algorithm lends itself to much more than just a shape-sensing tool. The inverse finite element framework allows for the solved nodal displacements to be used as prescribed displacements for calculating the full-field stresses and strains within the structure. This is the area in which the advantages of this method really start to become apparent.

Formulation

The theoretical foundation of the iFEM is primarily the minimization of a weighted least-squares smoothing functional that is expressed in terms of the unknown degrees of freedom (DOF) and known elemental strain data. The strain data that are incorporated into the iFEM include membrane, bending, and transverse shear components. Transverse shear cannot be directly determined from surface strain measurements; however, for most thin-shell structures, the transverse shear component is usually negligible, and can thus be neglected without sacrificing a great deal of accuracy. Note that the elemental strain data being used in the iFEM can come in the form of either experimental data or simulated strain data from a direct FEM program.

For a given triangular shell element of area A_e, three displacement and three rotation components are defined for each node as described by eq. (1).
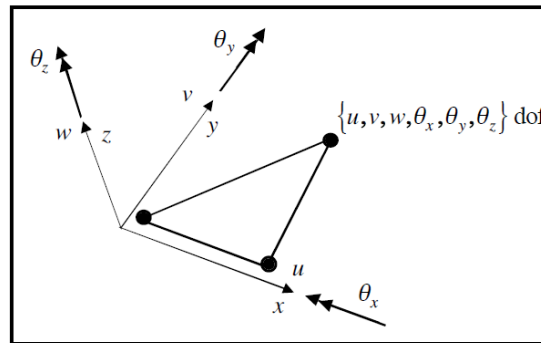
(Ref. 13)

$$u_x(x, y, z) \equiv u(x, y) + z\theta_y(x, y)$$
$$u_y(x, y, z) \equiv v(x, y) + z\theta_x(x, y)$$
$$u_z(x, y) \equiv w(x, y)$$
(1)

Corresponding to these displacement assumptions, the shell strain can be expressed as shown in eq. (2):

$$\begin{Bmatrix} \epsilon_{xx} \\ \epsilon_{yy} \\ \gamma_{xy} \end{Bmatrix} = \begin{Bmatrix} \epsilon_1 \\ \epsilon_2 \\ \epsilon_3 \end{Bmatrix} + z \begin{Bmatrix} \epsilon_4 \\ \epsilon_5 \\ \epsilon_6 \end{Bmatrix} \tag{2}$$

where the membrane strains, $e(u)$, and the bending strains, $k(u)$, are defined as shown in eqs. (3a) and (3b), respectively.
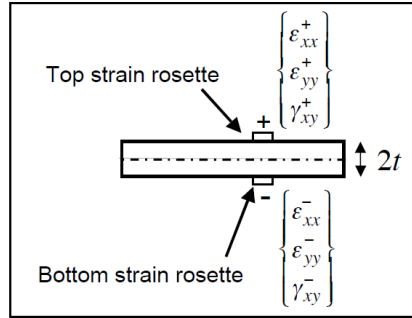
$$\begin{Bmatrix} \epsilon_1 \\ \epsilon_2 \\ \epsilon_3 \end{Bmatrix} \equiv \begin{bmatrix} \partial/\partial x & 0 & 0 & 0 & 0 \\ 0 & \partial/\partial y & 0 & 0 & 0 \\ \partial/\partial y & \partial/\partial x & 0 & 0 & 0 \end{bmatrix} \begin{Bmatrix} u \\ v \\ w \\ \theta_x \\ \theta_y \end{Bmatrix} = e(u) \tag{3a}$$

$$\begin{Bmatrix} \epsilon_4 \\ \epsilon_5 \\ \epsilon_6 \end{Bmatrix} \equiv \begin{bmatrix} 0 & 0 & 0 & 0 & \partial/\partial x \\ 0 & 0 & 0 & \partial/\partial y & 0 \\ 0 & 0 & 0 & \partial/\partial x & \partial/\partial y \end{bmatrix} \begin{Bmatrix} u \\ v \\ w \\ \theta_x \\ \theta_y \end{Bmatrix} = k(u) \tag{3b}$$

Additionally, the transverse shear-strains, $g(u)$, are defined as shown in eq. (3c).

$$\begin{Bmatrix} \epsilon_7 \\ \epsilon_8 \end{Bmatrix} = \begin{bmatrix} 0 & 0 & \partial/\partial x & 0 & 1 \\ 0 & 0 & \partial/\partial y & 1 & 0 \end{bmatrix} \begin{Bmatrix} u \\ v \\ w \\ \theta_x \\ \theta_y \end{Bmatrix} = g(u) \tag{3c}$$

For the case of the measured strain data, the shell strains are defined by eq. (4).

(Ref. 13)

$$\begin{Bmatrix} \epsilon_{xx} \\ \epsilon_{yy} \\ \gamma_{xy} \end{Bmatrix}^\epsilon = \begin{Bmatrix} \epsilon_1 \\ \epsilon_2 \\ \epsilon_3 \end{Bmatrix}^\epsilon + z \begin{Bmatrix} \epsilon_4 \\ \epsilon_5 \\ \epsilon_6 \end{Bmatrix}^\epsilon \tag{4}$$

where eqs. (5) and (6):

$$\begin{Bmatrix} \epsilon_1 \\ \epsilon_2 \\ \epsilon_3 \end{Bmatrix}^\epsilon = \frac{1}{2}\left(\begin{Bmatrix} \epsilon_{xx}^+ \\ \epsilon_{yy}^+ \\ \gamma_{xy}^+ \end{Bmatrix} + \begin{Bmatrix} \epsilon_{xx}^- \\ \epsilon_{yy}^- \\ \gamma_{xy}^- \end{Bmatrix} \right) \equiv e^\epsilon \tag{5}$$

$$\begin{Bmatrix} \epsilon_4 \\ \epsilon_5 \\ \epsilon_6 \end{Bmatrix}^\epsilon = \frac{1}{2t}\left(\begin{Bmatrix} \epsilon_{xx}^+ \\ \epsilon_{yy}^+ \\ \gamma_{xy}^+ \end{Bmatrix} - \begin{Bmatrix} \epsilon_{xx}^- \\ \epsilon_{yy}^- \\ \gamma_{xy}^- \end{Bmatrix} \right) \equiv k^\epsilon \tag{6}$$

4

The transverse shear strain component, $\boldsymbol{g}^{\epsilon}$, cannot be easily determined using surface strain measurements. Depending on the characteristics of the structure, all, or a subset of, the strain components are required. Elements in pure bending, and pure in-plane strains, require that only the strains on one surface be measured. In cases in which the surface sees a combination of bending and in-plane strain, the strains on both sides of the element are required. In the case of a wing, the skins are thin and see predominantly in-plane strains, requiring the user to measure only the strains on one side of the surface.

Using these element matrices, the weighted least-squares functional, eq. (7), is defined for a given triangular shell element of area A_e that bounds n strain sensors:

$$\Phi_e(\mathbf{u}) = w_e \|\mathrm{e}(\mathbf{u}) - \mathrm{e}^{\varepsilon}\|^2 + w_k \|\mathrm{k}(\mathbf{u}) - \mathrm{k}^{\varepsilon}\|^2 + w_g \|\mathrm{g}(\mathbf{u}) - \mathrm{g}^{\varepsilon}\|^2 \tag{7}$$

where the squared norms are least-squares difference terms defined as shown in eqs. (8)-(10).

$$\|\mathbf{e}(\mathbf{u}) - \mathbf{e}^{\varepsilon}\|^2 = \frac{1}{n} \iint_A \sum_{i=1}^{n} [\mathbf{e}(\mathbf{u})_i - \mathbf{e}_i^{\varepsilon}]^2 \, dxdy \tag{8}$$

$$\|\mathbf{k}(\mathbf{u}) - \mathbf{k}^{\varepsilon}\|^2 = \frac{(2t)^2}{n} \iint_A \sum_{i=1}^{n} [\mathbf{k}(\mathbf{u})_i - \mathbf{k}_i^{\varepsilon}]^2 \, dxdy \tag{9}$$

$$\|\mathbf{g}(\mathbf{u}) - \mathbf{g}^{\varepsilon}\|^2 = \frac{1}{n} \iint_A \sum_{i=1}^{n} [\mathbf{g}(\mathbf{u})_i - \mathbf{g}_i^{\varepsilon}]^2 \, dxdy \quad \text{or}$$

$$\|\mathbf{g}(\mathbf{u}) - \mathbf{g}^{\varepsilon}\|^2 = \iint_A \sum_{i=1}^{n} [\mathbf{g}(\mathbf{u})]^2 \, dxdy \tag{10}$$

In the functional shown in eq. (7), w_e, w_k, and w_g are positive weighting constants associated with a given shell element. These constants effectively determine the extent to which each of the strain components of the element are constrained to their measured values. Each of these weighting constants serve to ensure stable performance even when strain values are not taken from every finite element used in the structure. For elements in which no strain data are being taken, a value of 10^{-6} is assigned to each weighting constant. It should be noted that for a given element, the value of each weighting constant can be individually specified depending on the availability of measured strain data corresponding to each strain component. Inspection of eq. (7) reveals that the least-squares operation undertaken by the iFEM serves to integrate and smooth the measured strain data.

Once the least-squares functional is defined for each element, the sum of all N element functionals is minimized with respect to the unknown displacement DOF, as shown in eq. (11).

$$\frac{\partial}{\partial \boldsymbol{u}} \sum_{e=1}^{N} \Phi_e(\boldsymbol{u}) = 0 \tag{11}$$

The variational statement given in eq. (11) results in a linear system of equations that can be solved for the unknown DOF provided that appropriate displacement boundary conditions have been imposed.

Implementation Framework

The work presented in this report implements the iFEM using a three-node triangular shell element adopted from references 12-14. Each node has six DOF. The formulation was implemented into the MATLAB® code as seven main components plus additional error analysis and plotting tools. The seven main components are shown in the box elements in the high-level overview outlining the entire iFEM

implementation process that is figure 1. Figure 1 facilitates an understanding of the process and results presented in this report.

Mesh Generation: MSC Patran Software (Pre-Processor)

The iFEM process uses a conventional FEM modeling concept. As an alternative to writing an independent pre- and post-processor for handling the mesh generation, it was determined that using an off-the-shelf preprocessor for the finite element model generation would be the expedient approach. The MSC Patran software (MSC Software Corporation, Newport Beach, California) (ref. 21) was selected for mesh generation of the wing. The mesh generation phase is the only aspect not put into the MATLAB® code.

The mesh generation process, described in more detail below, basically entails using a computer-aided design (CAD) model in addition to the instrumentation locations and creating a triangular-node FEM surface mesh. The instrumentation sensors, which are typically strain gages and fiber optic sensors, are usually modeled as one-dimensional bar elements. The MSC Patran software also simplified the process of defining boundary conditions such as constraints and nodal load application points.

Direct FEM Code or Experimental Strain Data

There are two options for producing strains for the iFEM approach: 1) obtain strain data from an experimental loads or thermal test; or 2) obtain predicted strain results from a finite element code. The direct FEM allows the user to produce predicted strains for different loading conditions before a test is performed. The direct code is no different than what an off-the-shelf code such as MSC Nastran (MSC Software Corporation, Newport Beach, California) (ref. 21) would produce.

The direct component solves the conventional direct finite element problem for the nodal displacements given the element properties and boundary conditions. The direct FEM code requires input of the node locations, mesh connectivity, material properties, boundary conditions, and applied loading. The direct FEM outputs nodal displacements and element strain data for input into the iFEM code.

Noise Generator

Most strain sensors contain a certain level of noise in the signal. To adequately test the iFEM approach it is prudent to apply a certain level of noise to the predicted strain results. The noise generator simulates the presence of experimental noise on the measured strain values prior to input into the iFEM code. Noise is created by adding a random number within some user-specified range to the value of each strain component associated with each finite element. If strain data are from experimental measurements, this step is unnecessary.

Strain Solver

The strain data taken from a test are usually from axial strain sensors such as a single strain gage or a fiber optic sensor. The iFEM method utilizes shear strains and axial strains. The strain solver converts axial strain data from the strain gage or fiber optic sensor into rosette strains defining the strains for each finite element. Three independent strains oriented at different angles to each other are required for the transverse shear strain calculation (ref. 22).

iFEM Code

The iFEM code uses the strain data obtained from experimental measurements or the direct FEM code to perform the weighted least-squares operation and calculate the unknown DOF. It is important to note that material property data are not required. The iFEM code outputs nodal displacement and element strain

data for comparison to direct FEM results. The iFEM code only requires nodal locations, connectivity, boundary constraints, and element strain data. Figure 2 shows a 3-D plot of the original mesh (green), the direct FEM solution (blue), and the iFEM solution (red).

Prescribed Displacements

The prescribed displacements process performs the direct FEM on a refined mesh using the prescribed nodal displacements calculated by the iFEM. The iFEM requires a less-refined mesh compared to what may be required for an in-depth stress evaluation. The prescribed displacements process obtains the full-field stress, strain, displacement, and loading on a refined mesh.

Loads Calculator

It is important to understand the loads within a structure. Most aerospace structures are designed using shear, bending, and torque loads. The loads calculator calculates the reaction loads based on the iFEM nodal displacements. Once the reaction loads are calculated, the wing shear, bending, and torque loads can be derived. The reaction loads calculation can be performed at any spanwise location on the wing.

Test Article Description

The test article is a 30-ft half-span straight wing with two spars; the test article is constrained at the wing root. The wing is instrumented with both fiber optic strain sensors and metallic foil strain gages. On the lower surface of the wing, a single FOSS fiber is positioned on both the leading- and trailing-edge spars. The lower surface also features a central array of FOSS fibers positioned in a trapezoidal fashion in the region bounded by the leading- and trailing-edge spars. On the upper surface of the wing, a single FOSS fiber is oriented above the location of the trailing-edge spar. Spanwise, fiber optic strain sensors are oriented in a triangular rosette pattern in the region bounded by the leading- and trailing-edge spars. Note that in all cases, the FOSS is placed on the exposed surface of the wing; no sensors are located within the interior regions of the structure. Metallic foil strain gages are installed at five spanwise stations on the spars and wing skins. The gages are not planned to be used in the iFEM investigation.

Modeling and Mesh Generation Process

The iFEM implementation was performed on the half-span test wing wing shown in figures 3 and 4. Also shown in these images are the FOSS fibers and 3-D laser scan targets. A close-up image of the 3-D laser scan targets is given in figure 5. A major component of the iFEM workflow is the generation of a mesh used to represent the structure. Here, the mesh was generated using the MSC Patran software; all surfaces were discretized using three-node triangular shell elements.

After generating a CAD model of the test wing (fig. 6) using the 3-D laser scan, the physical structure was outfitted with an array of fiber optic strain sensors (as shown in fig. 3). After instrumenting the wing, junctions at which two or more FOSS fibers met were identified and marked using 3-D laser scan targets (fig. 5). The locations of these targets were picked up using a 3-D laser scanning system and were then used to generate a point cloud (fig. 7) with points whose coordinates corresponded to the location of the targets on the physical wing.

When generating the point cloud, it is important to use a coordinate system that is common to both the CAD model and the point cloud. With these coordinate systems matched, the point cloud is simply overlaid onto the CAD model and connected with curves to represent the location of the fiber optic strain sensors. In order to generate triangular rosette patterns on the lower surface of the wing, the central array of trapezoidal fiber optic strain sensors was further subdivided using a series of triangles. Next, a series of planes (oriented parallel to the longitudinal axis of the aircraft) was defined at each of the points used to

subdivide the trapezoidal FOSS arrays along the wing span. Using these planes, points were defined at the intersection of each plane with the leading edge, trailing edge, leading-edge spar, and trailing-edge spar.

After defining all points in the MSC Patran software, the point locations were defined to be finite element nodes. Note that planes were used to define the locations of these nodes in order to ensure that at several specified spanwise positions there existed a node on both the leading and trailing edges that shared the same spanwise coordinate. This relationship enables the definition and calculation of the twist experienced by the loaded wing. After defining the nodal positions on both the upper and lower surfaces, the mesh of the structure was generated by connecting the nodes with three-node triangular shell elements. This is shown in figure 8. All surfaces, including the skin and wing spars, were meshed using triangular shell elements. Since fiber optic strain sensors can only capture axial strain data, their defining curves were meshed using one-dimensional Bar2 (axial deformation only) elements.

Model Characteristics

For the purposes of the direct FEM analysis, all shell elements were assumed to be composed of a material having an elastic modulus of 10^6, a Poisson's ratio of 0.33, and a thickness of 0.1 in. To simplify the analysis, the presence of fairings and control surfaces was neglected in modeling the structure. Figure 9 shows the completed FEM model including the FOSS configuration shown in figures 2 and 3; this model was used for all code validation and analysis performed in the implementation of the iFEM.

Boundary Conditions

Two load cases were chosen for the purposes of this report. The first load case was a single transverse static tip load of 1500 lb located at the wing tip on the forward spar lower cap node. The second load case was a distributed load with a series of 500-lb magnitude transverse static loads positioned on 16 nodes on the lower surface leading edge.

Results

One of the goals of the iFEM is to reconstruct accurately the displacement and twist of a wing that has been subjected to an arbitrary load condition. Wing displacement is simply quantified by the change in vertical position of a given node before and after the deformation. For a given spanwise station, wing twist is defined using the inverse tangent relationship. Figure 10 graphically shows the relationship. The wing twist angle is calculated based on eq. (12), where θ_i defines the twist angle at a given spanwise station, δ_{fwd} defines the displacement of the leading-edge node at a given spanwise station, δ_{aft} defines the displacement of the trailing-edge node at a given spanwise station, and c_i defines the local chord length.

$$\theta_i = \tan^{-1}\left(\frac{\delta_{fwd} - \delta_{aft}}{c_i}\right) \qquad (12)$$

Various error measures are examined in this report. The displacement residual is defined by y_i, where x_i is the direct FEM or MSC Nastran value (either displacement or wing twist angle), x'_i is the iFEM-derived value, and n is the number of measurements. The equation for load residual is shown in eq. (13) and that for the mean error in eq. (14). Equations for the standard deviation, percent difference, and mean percent difference are calculated as shown in eq. (15), eq. (16), and eq. (17), respectively.

$$y_i = x'_i - x_i \qquad (13)$$

$$Mean\ Error = \frac{1}{n}\sum_{i=1}^{n}(x' - x_i) \qquad (14)$$

$$\sigma = \sqrt{\frac{1}{n-1}\sum_{i=1}^{n}(y_i - \bar{y}_i)^2} \tag{15}$$

$$PD_i = \left|\frac{x'_i - x_i}{x_{Max}}\right| * 100 \tag{16}$$

$$MPD = \frac{1}{n}\sum_{i=1}^{n}(PD_i) \tag{17}$$

The validity of the results (nodal displacements, wing twist, stress) predicted using the iFEM was assessed by comparison to the results generated using the direct FEM. Both the direct and inverse FEM procedures are in the form of in-house MATLAB® routines. Before proceeding, validation of the results given by the NASA in-house direct FEM code were performed by comparison to the results generated by the MSC Nastran code. Validation of the NASA direct FEM code were performed using the two load cases described above.

As shown in figure 11, figure 12, and table 1, the wing displacement values generated using the in-house direct FEM code are in close agreement with the values generated using MSC Nastran code; thus, the nodal displacement values provided by the NASA direct FEM code are considered validated. All comparisons and error calculations of iFEM results were made with respect to this validated in-house direct FEM code.

Table 1. Percent error between MATLAB® direct FEM and MSC Nastran nodal displacements.

Direct FEM code results						
Applied load	Deformation	Value at wing tip, in.	Maximum error, in.	Mean error, in.	Std dev, in.	MPD, %
Tip	Displacement	12.01	0.40	-0.12	0.13	0.95
Distributed	Displacement	22.97	0.54	-0.15	0.18	0.66

Sensor Configuration

For practical reasons, outfitting the entire structure, particularly the interior of the structure, with strain gages or fiber optic strain sensors is usually not feasible. Moreover, in certain situations such as aerodynamic tests, placing sensors on the leading and trailing edges of the wing is also not ideal. Thus, one of the focuses of the present analysis is to investigate the sensor configurations (that is, to determine where strain data should be taken) needed to best characterize the deformed shape of the structure while simultaneously taking into account accuracy and feasibility considerations. The configurations tested include the full set of finite elements, the perimeter elements, central rosette elements, and the upper and lower surface elements. A visual representation of each configuration scheme is given in figures 13-16. Note that the upper/lower surface element configuration differs from that of the full-set configuration in that it does not include the leading edge, trailing edge, leading-edge spar, or trailing-edge spar elements. Each sensor configuration was subjected to two loading conditions, a static transverse tip load, and a constant static load distribution acting on the wing leading-edge spar.

Figures 17-20 and figures 21-24 show the wing displacement and twist values that result from using full set, upper and lower surface; perimeter; and center rosettes and axial strain sensor configurations. The wing displacement and twist error values are shown in tables 2 and 3. As seen in figure 17 and figure 21 taking strain data from all finite elements in the model results in wing displacement and wing twist values that are in strong agreement with those generated using the direct finite element method. While difficult to implement in an actual structure, this sensor configuration serves to validate the displacement and twist data predicted using the iFEM.

Table 2. Wing displacement percent errors for various strain element configurations.

Sensor configuration errors, displacement						
Applied load	Sensor configuration	Value at wing tip, in.	Maximum error, in.	Mean error, in.	Std dev, in.	MPD, %
Tip	Full set	12.01	0.00	0.00	0.00	0.00
Tip	Upper and lower surface	12.01	0.00	0.00	0.00	0.02
Tip	Perimeter	12.01	0.01	0.00	0.00	0.03
Tip	Center rosette and axial strain	12.01	0.04	-0.02	0.01	0.13
Distributed	Full Set	22.97	0.00	0.00	0.00	0.00
Distributed	Upper and lower surface	22.97	0.00	0.00	0.00	0.00
Distributed	Perimeter	22.97	0.05	-0.03	0.02	0.14
Distributed	Center rosette and axial strain	22.97	0.11	-0.07	0.04	0.31

Table 3. Wing twist percent errors for various strain element configurations.

Sensor configurations errors, wing twist angle						
Applied load	Sensor configuration	Value at wing tip, deg	Maximum error, deg	Mean error, deg	Std dev, deg	MPD, %
Tip	Full set	0.61	0.00	0.00	0.00	0.00
Tip	Upper and lower surface	0.61	0.02	-0.01	0.01	1.34
Tip	Perimeter	0.61	0.03	0.00	0.01	1.94
Tip	Center rosette and axial strain	0.61	0.11	-0.02	0.03	3.97
Distributed	Full set	1.32	0.00	0.00	0.00	0.00
Distributed	Upper and lower surface	1.32	0.01	-0.01	0.00	0.30
Distributed	Perimeter	1.32	0.11	-0.05	0.04	3.01
Distributed	Center rosette and axial strain	1.32	0.31	-0.18	0.12	9.82

It is observed that all sensor configurations give accurate shape comparisons to the direct method predictions. As the sensor configuration is minimized, it is observed that the twist comparisons degrade. This is to be expected and one could refine the mesh and add more instrumentation to improve this comparison. It is recommended for future experiments to locate rosettes around the perimeter as demonstrated with the perimeter sensor configuration.

Effect of Noisy Strain Measurements on iFEM Solution Accuracy

The iFEM is ultimately intended for use on real engineering projects in which the measured strain data being input into the iFEM code are influenced by noise. To assess the effect of noise on the values given by the iFEM, strain measurements for the full-set and upper-and-lower surface sensor configurations will be repeated using element strain data that have been affected by random errors ranging between -5% and 5%, and between -10% and 10%. For a given element and membrane strain component (E_x, E_y, E_{xy}), upper and lower bounds for the random errors were calculated. For each membrane strain component of each element, a random number was generated between the upper and lower error boundaries. This random number was then added to the original strain value to simulate the presence of experimental noise on the

gathered strain data prior to input into the iFEM code. This randomly generated noise value was implemented on the E_x, E_y, and E_{xy} strain components. The effect of 10 percent random noise on the strain values (E_x, E_y, E_{xy}) input into the iFEM code for a distributed load are shown in figure 25. Figures 26-30 and Table 4 highlight the noise results for different sensor configurations.

Table 4. Noise results for various strain element configurations.

Noise results								
Applied load	Sensor configuration	Percent noise	Deformation	Value at wing tip	Maximum error	Mean error	Std dev	MPD, %
Distributed	Full set	10	Displacement	22.97 in.	0.03 in.	0.02 in.	0.01 in.	0.09
Distributed	Upper and lower surface	10	Displacement	22.97 in.	0.1 in.	0.03 in.	0.04 in.	0.18
Distributed	Perimeter	10	Displacement	22.97 in.	0.11 in.	0.03 in.	0.03 in.	0.14
Distributed	Full set	10	Twist	1.32 deg.	0.03 deg.	-0.01 deg.	0.01 deg.	0.53
Distributed	Upper and Lower surface	5	Twist	1.32 deg.	0.64 deg.	0.24 deg.	0.19 deg.	13.99

As expected, the full-set sensor configuration produces accurate results with the addition of 10 percent noise. The upper-and-lower-surface and perimeter sensor configurations also produce accurate results with noise for the displacement comparisons. The twist comparison for the full-set configuration with noise produces similar results, as expected. Larger errors are observed for the upper-and-lower-surface twist comparison. The conclusion to be drawn is that to accurately measure twist it is necessary to add additional strain sensors to the surface and refine the mesh, and or add sensors to the spars.

Calculation of Reaction Loads

Load monitoring can be an important tool for validating computational fluid dynamic models in flight. The NASA AFRC has a long history of monitoring aircraft loads in flight for envelope expansion and model validation activities (ref. 22) The typical approach used on past projects consists of an aircraft wing instrumented with strain gages that can monitor the shear, bending, and torque loads in the wing at one or two spanwise wing stations (ref. 23) The strain gages are usually located on the spar webs for shear, spar caps for bending, and wing skins for torsion loads. The strain gages are correlated during a ground test by applying known loads to the structure. The applied loads are typically in the form of hydraulic rams or shot bags. With the introduction of FOSS and iFEM methods, there is the possibility that the spanwise shear, bending, and torque loads can be measured in real time, creating new additional insight into the structure.

The present study attempts to calculate the shear bending and torque wing loads at the root wing station(figure 31). This approach could easily be expanded across the entire wing span for future applications. The process works by using the iFEM nodal displacements to calculate the reaction loads at the nodal constraints. The nodal reaction loads for the direct and iFEM results are shown in figures 32-34 for three different sensor configurations. The reaction loads are then converted to shear, bending, and torque loads at that station. Table 5 shows the calculated loads and percent errors for the three different sensor configurations and for two different constraint conditions. As expected, the full iFEM sensor configuration produced less than 1 percent difference to the direct results. The surface and perimeter configurations were adequate for calculating shear and bending loads. Torsion load errors were much larger for the surface and perimeter configurations, but this is probably due to the low magnitude of torsion loads being put into the wing. It is expected that with improved modeling considerations and wings with greater torsion loading, that iFEM would produce adequate results for measuring torsion. This study calculated the loads at one wing station; to obtain the spanwise distributions, one would simply model the wing with multiple spanwise stations and calculate the nodal reaction loads at each station.

Table 5. Shear bending and torque loads calculated at the wing root station.

Reaction load comparison							
All constraints							
	Calculated load				Error, %		
	Direct	Full set	Surface	Perimeter	Full set	Surface	Perimeter
Shear, lb	7500	7543	6638	7776	0.58	-11.49	3.67
Bending, in-lb	1465006	1465004	1459002	1457922	0.00	-0.41	-0.48
Torque, in-lb	68719	68356	25008	4018	-0.53	-63.61	-94.15
Spar constraints							
	Calculated load				Error, %		
	Direct	Full set	Surface	Perimeter	Full set	Surface	Perimeter
Shear, lb	7500	7530	7301	10969	0.41	-2.66	46.25
Bending, in-lb	1463536	1463534	1468219	1473523	0.00	0.32	0.68
Torque, in-lb	68719	68204	89624	4644	-0.75	30.42	-93.24

Conclusions

The purpose of this report is to provide a status of the work to date regarding the implementation of the inverse Finite Element Method (iFEM) into the MATLAB® (The MathWorks, Inc., Natick, Massachusetts) code for calculating structural deformation (including both displacement and wing twist) and internal loading of aerospace structures. Theory and framework were discussed, along with the results from a half-span wing model. Several accomplishments and conclusions can be derived from this report.

This report described a representative finite element model of a half-span test wing article for assessing and investigating the iFEM implementation procedure. The complete process of instrument installation and laser correlation to a 3-D computer-aided design (CAD) model along with the finite element mesh generation was accomplished, producing a finite element sensor layout that corresponds appropriately to the as-installed sensor configuration.

A three-node shell element formulation was implemented into the MATLAB® code in both a direct (conventional) and an iFEM approach for efficient modeling and analysis of aerospace structures and instrumentation monitoring schemes. The iFEM is based primarily on the minimization of a weighted least-squares smoothing functional that is expressed in terms of the unknown degrees of freedom and known elemental strain data. The iFEM was shown to work when sparse strain data are available through the use of penalty parameters. The direct MATLAB® code implementation was validated to within 1 percent against a commercial FEM code. Similarly, by taking strain data from all finite elements, the nodal displacement and wing twist values predicted using the iFEM were validated by comparison to the direct FEM results. Using several sensor configuration schemes, the effect of sparse measured strain data on the predicted displacement, twist, and loading predicted using the iFEM was evaluated by comparison to the results generated using the direct FEM. Additionally, noise effects were investigated to adequately assess the influence of the instrumentation system on the calculated nodal displacement and wing twist values. Finally, the reaction loads were calculated to show the ability to calculate the spanwise wing load distributions.

The iFEM approach is shown to be a robust, computationally efficient method that is well suited for real-time measurement of real-time structural deformation and loads. The results from this study have provided insight into the method itself and for future aerospace vehicle applications.

Figures
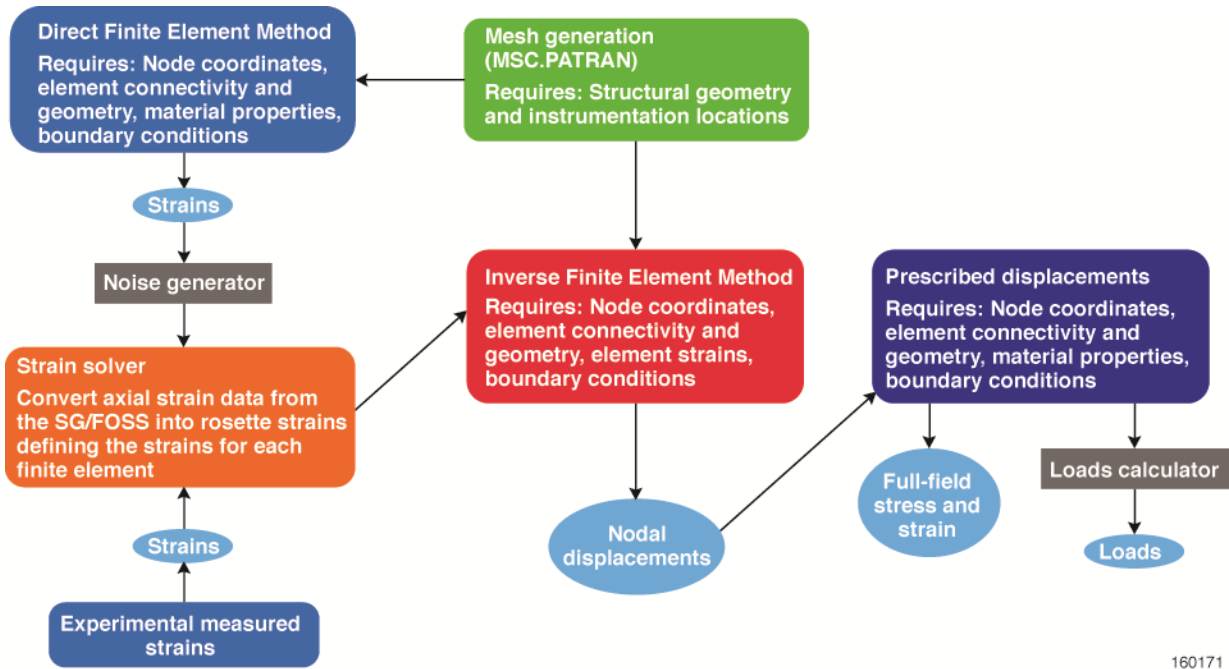
Figure 1. MATLAB® implementation framework.
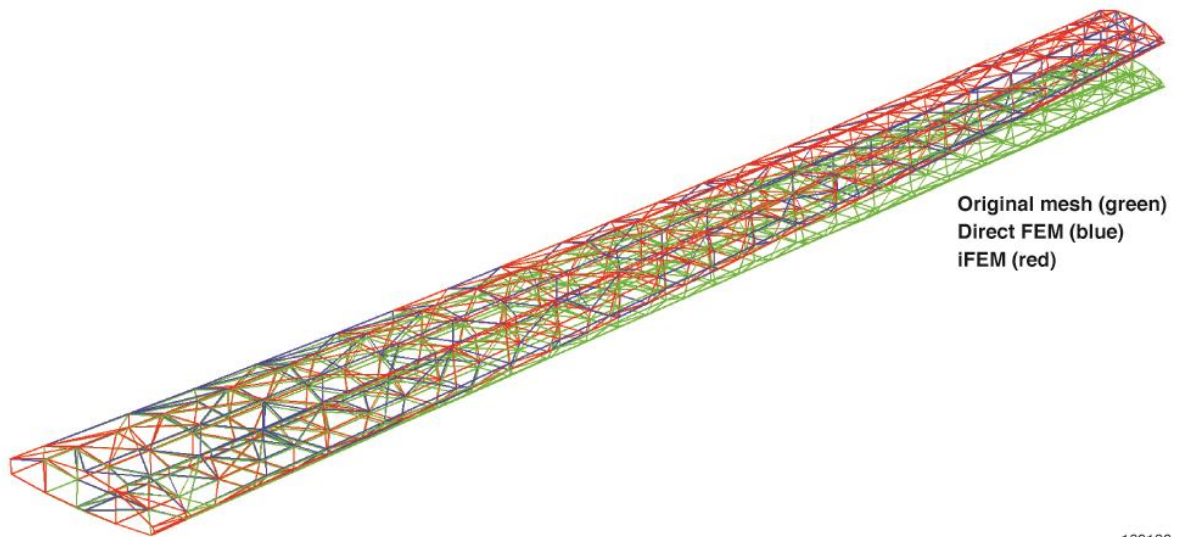
Figure 2. Direct versus iFEM 3-D plot.
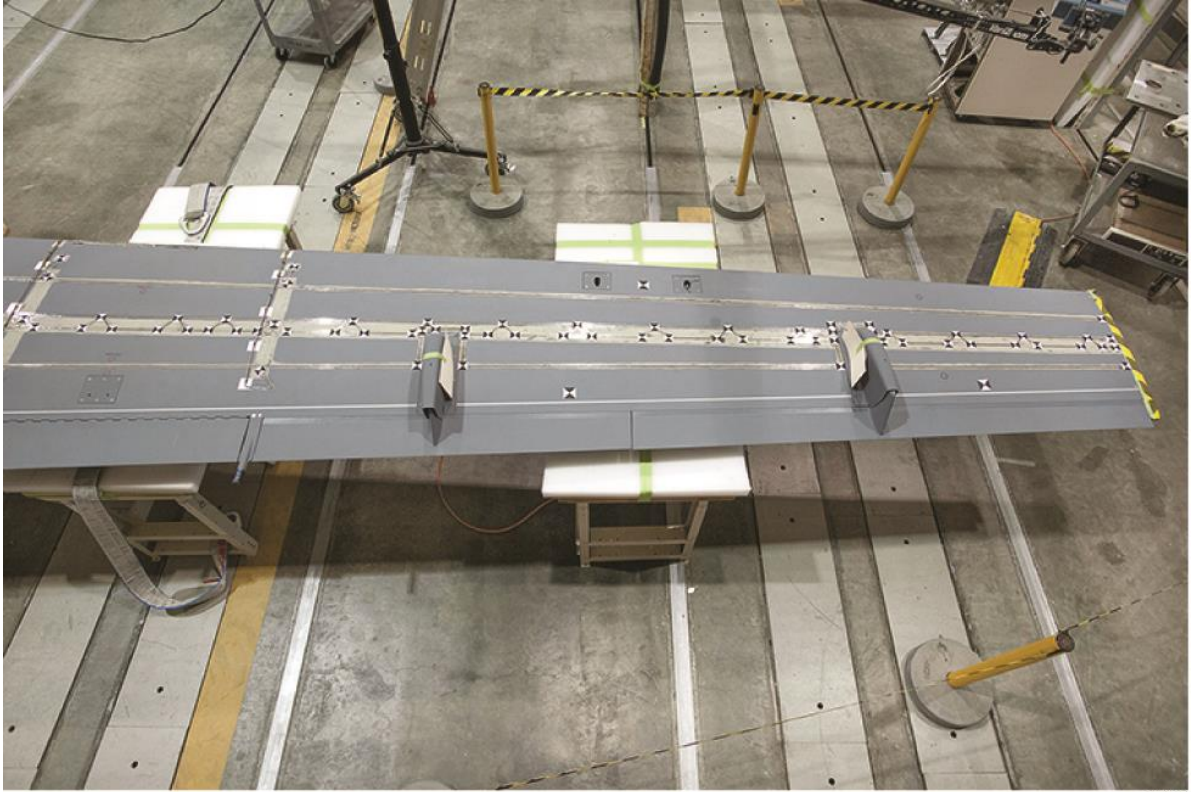
Figure 3. Test wing lower surface with FOSS and 3-D laser scan targets visible.
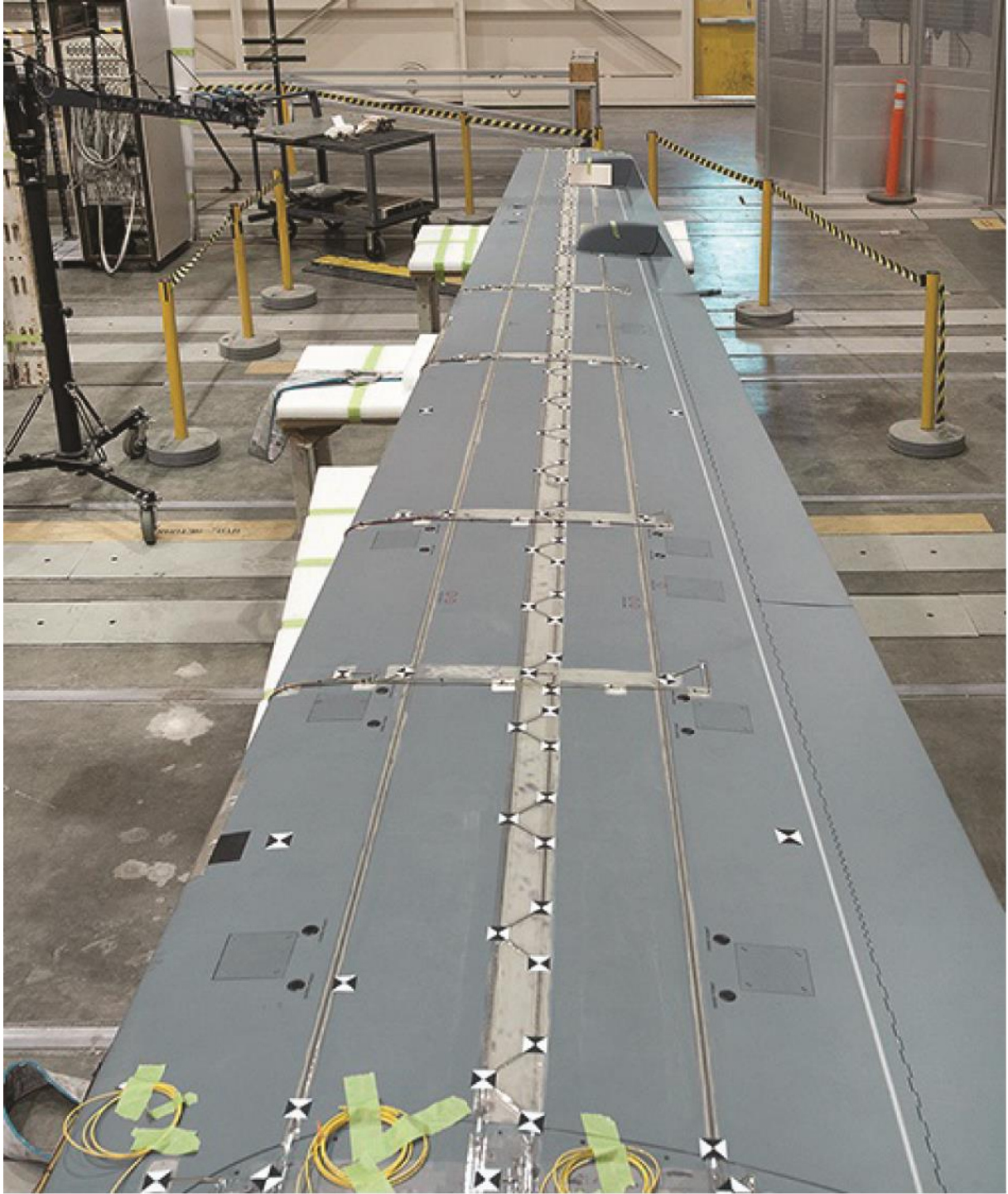
Figure 4. Spanwise view of test article.
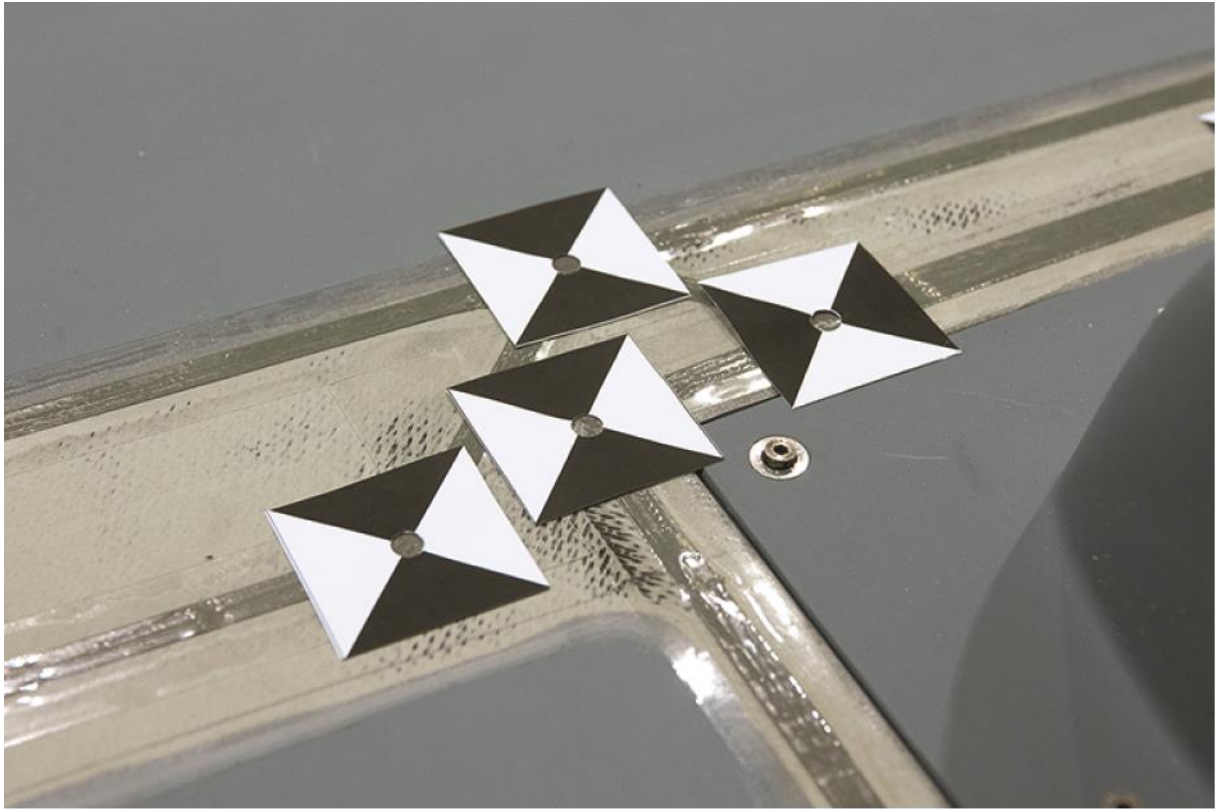
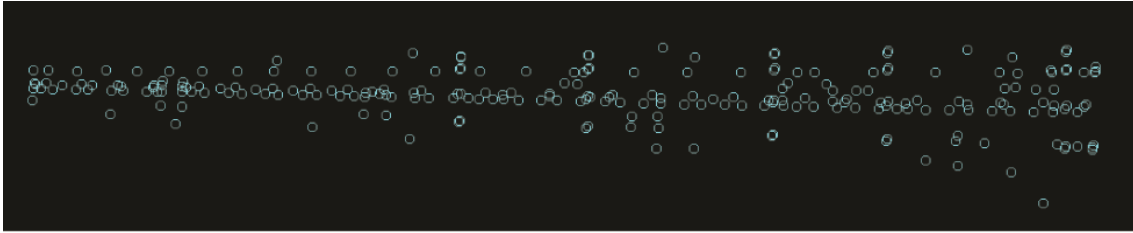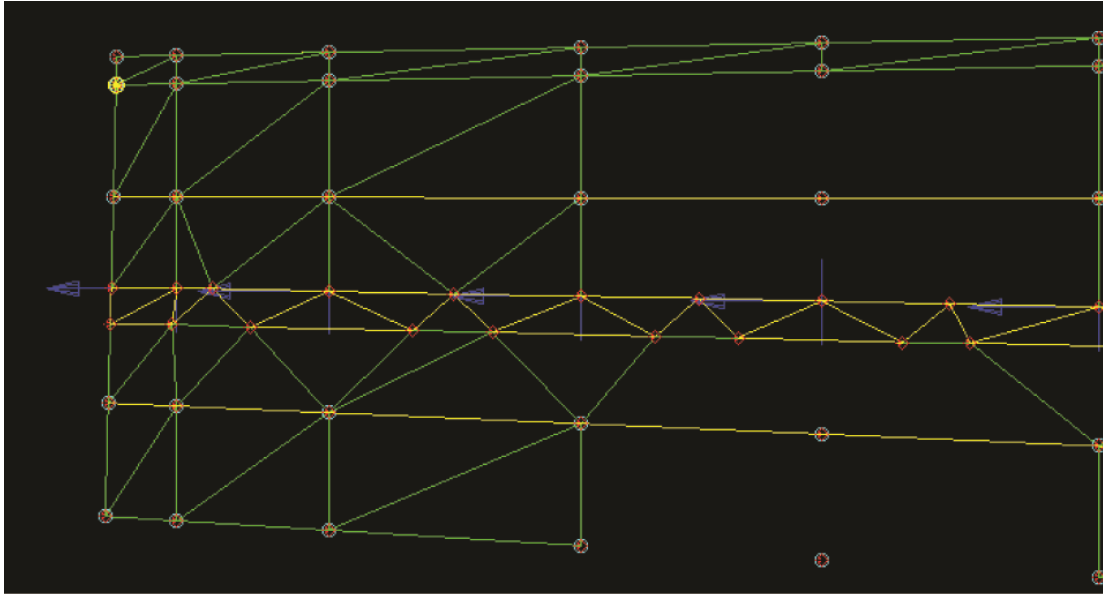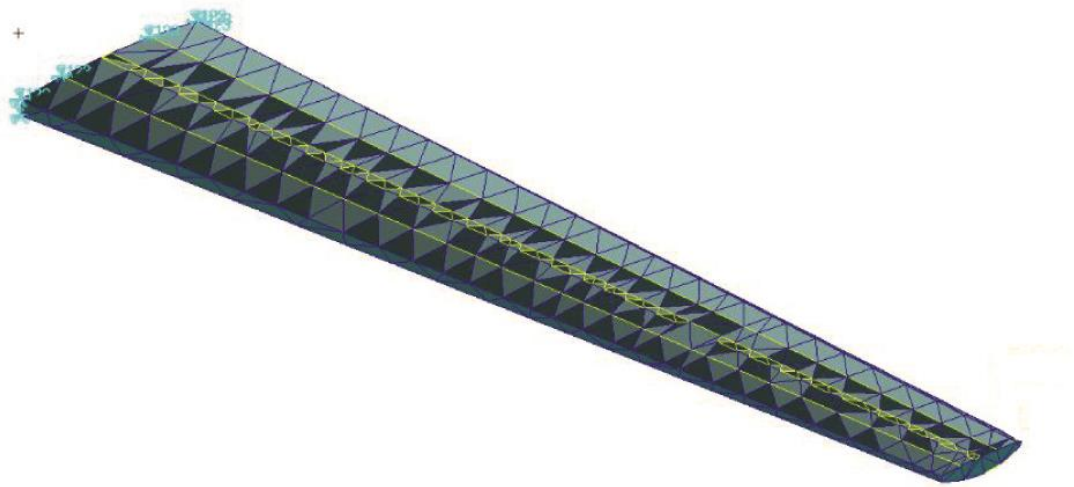Figure 5. Close-up view of 3-D laser scan targets.
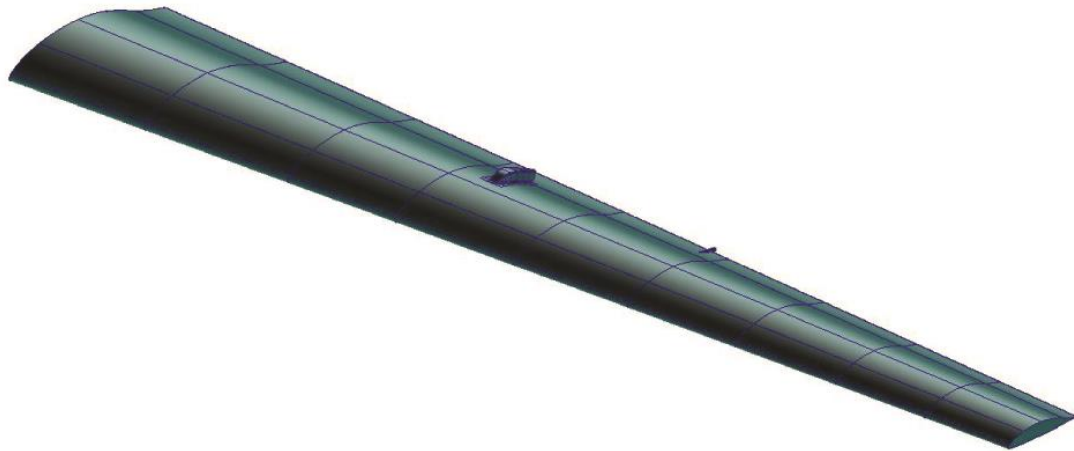
Figure 6. CAD model of test wing.

Figure 7. Instrumentation target point cloud generated by using 3-D laser scan.

Figure 8. Partial wing mesh showing node locations, triangular shell elements, and axial bar elements.

Figure 9. FEM model of test wing.
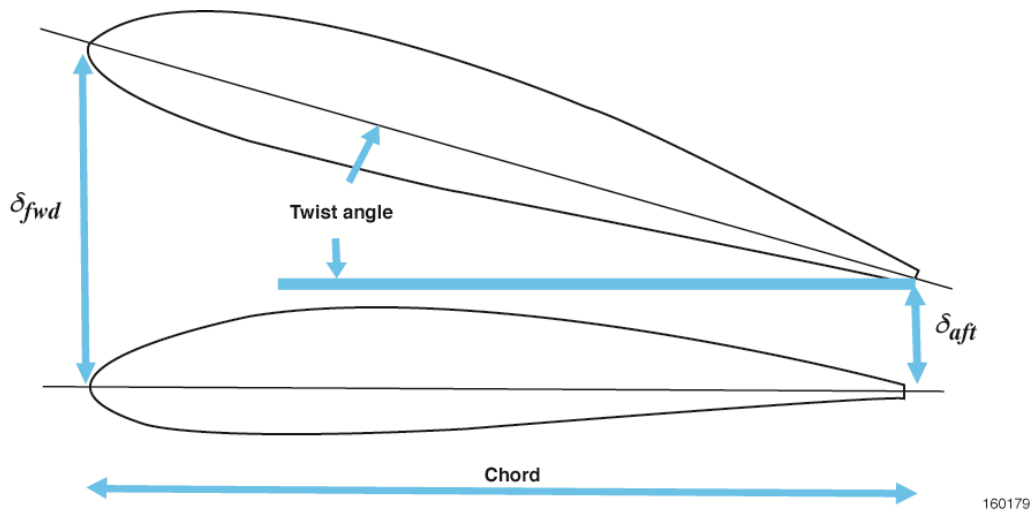
Figure 10. Wing twist calculation.
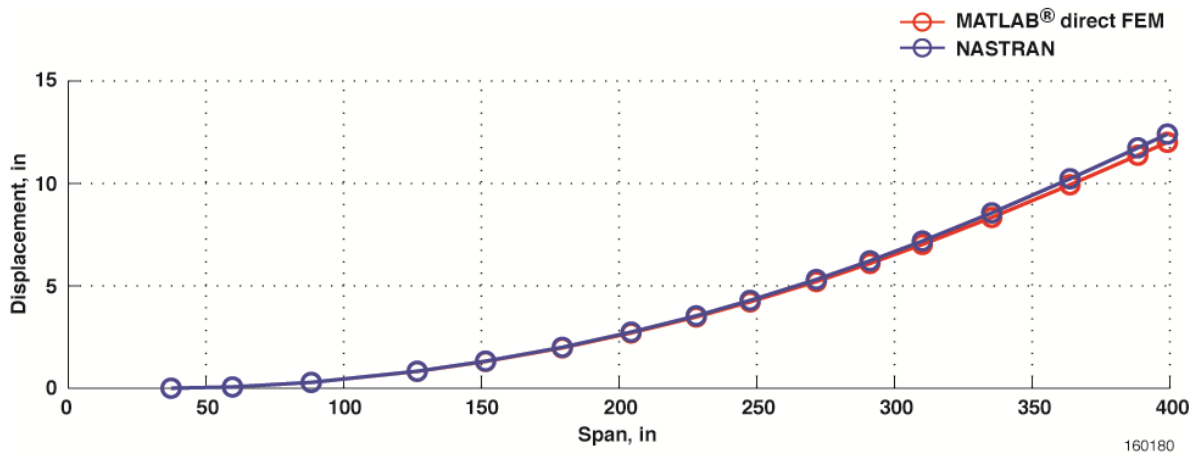
Figure 11. Validation of MATLAB® direct FEM nodal displacements (tip load).
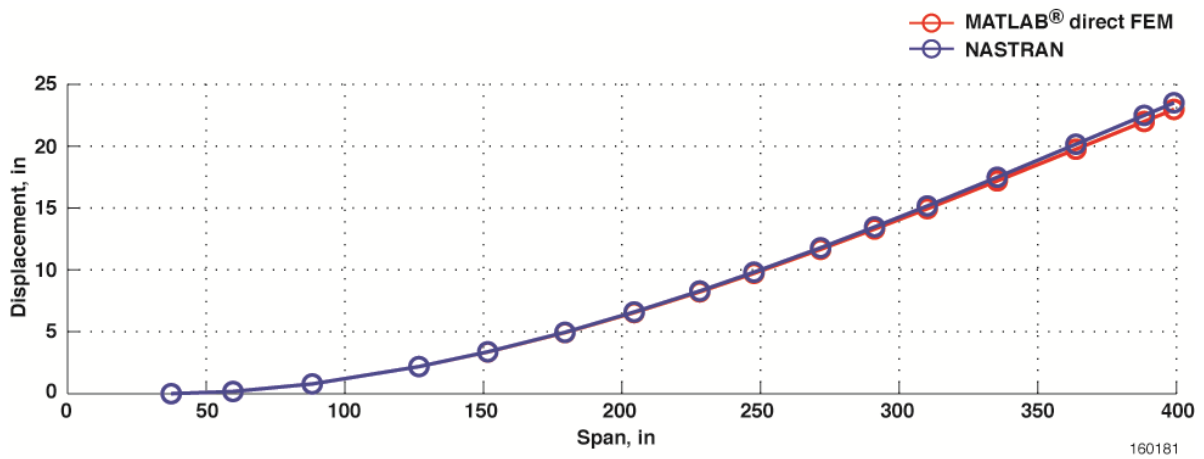
Figure 12. Validation of MATLAB® direct FEM nodal displacements (constant distributed load).

18
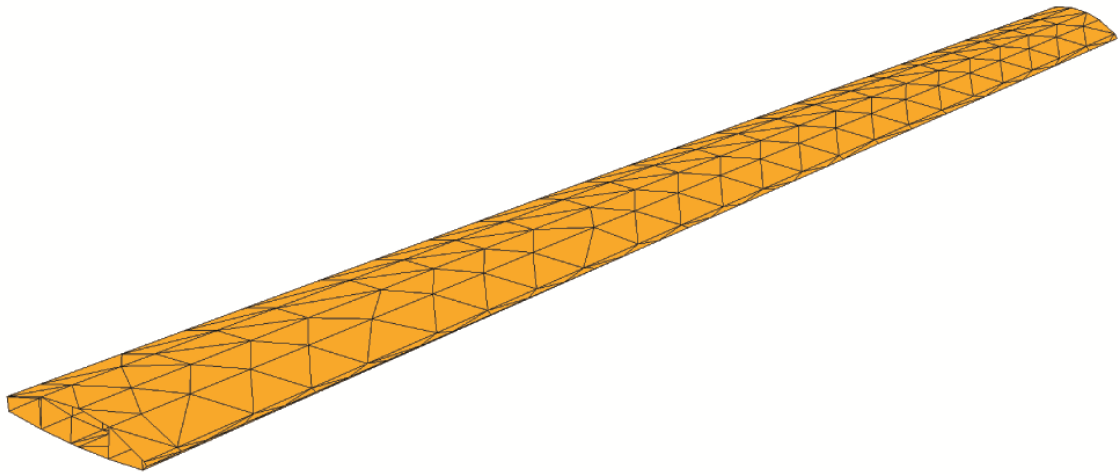
160182

Figure 13. Full set strain element configuration.
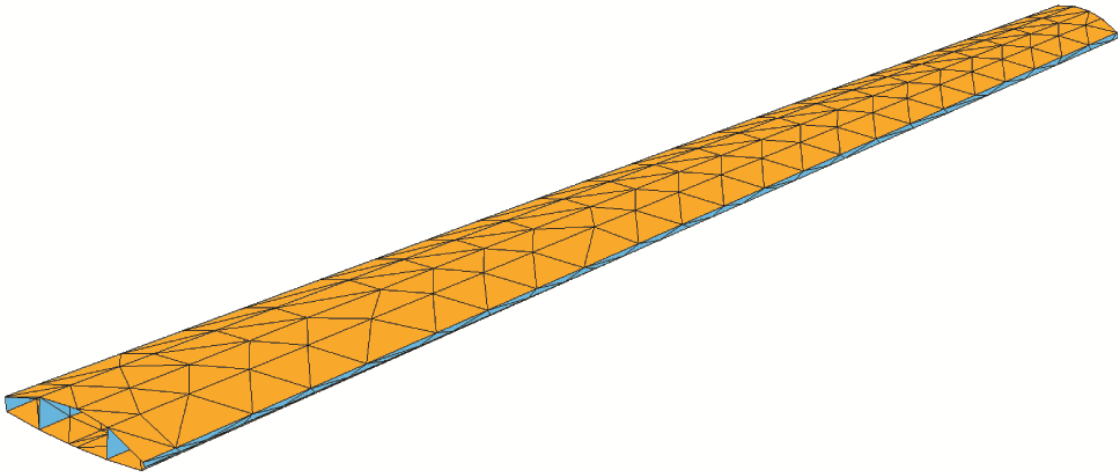
160183

Figure 14. Upper and lower surface strain element configuration.
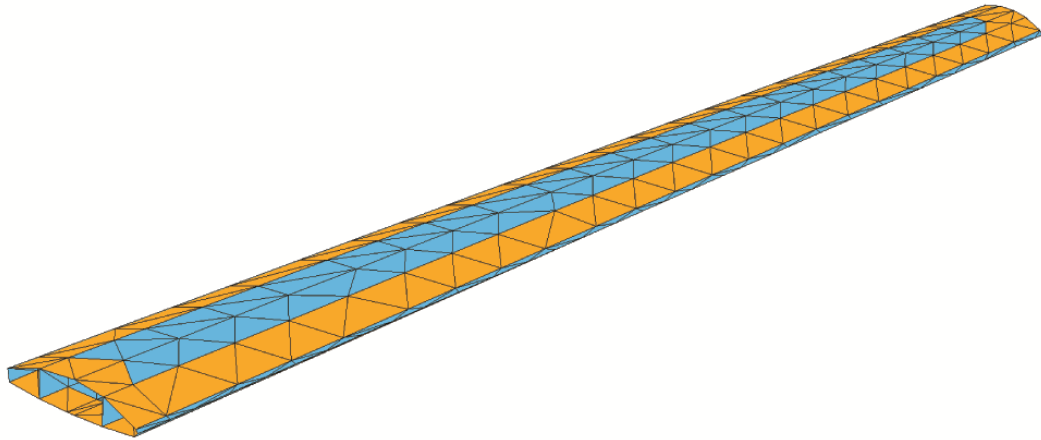
Figure 15. Perimeter strain element configuration.
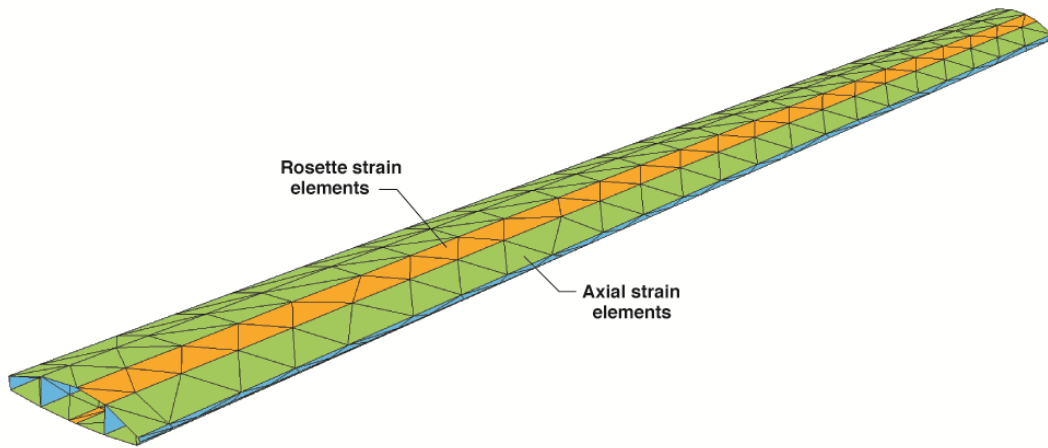
Figure 16. Central rosettes and axial strain element configuration.
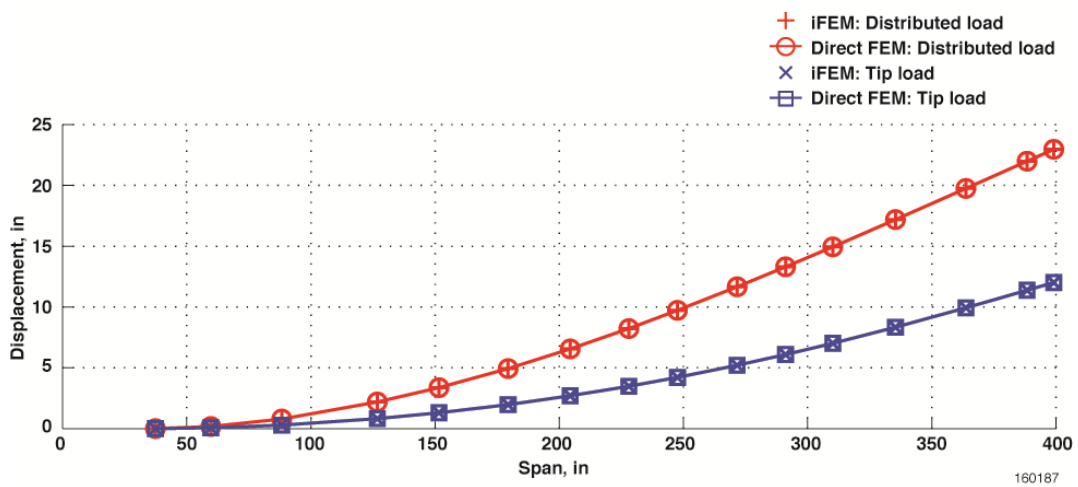
Figure 17. iFEM versus direct FEM displacements (sensor configuration = full set).

20
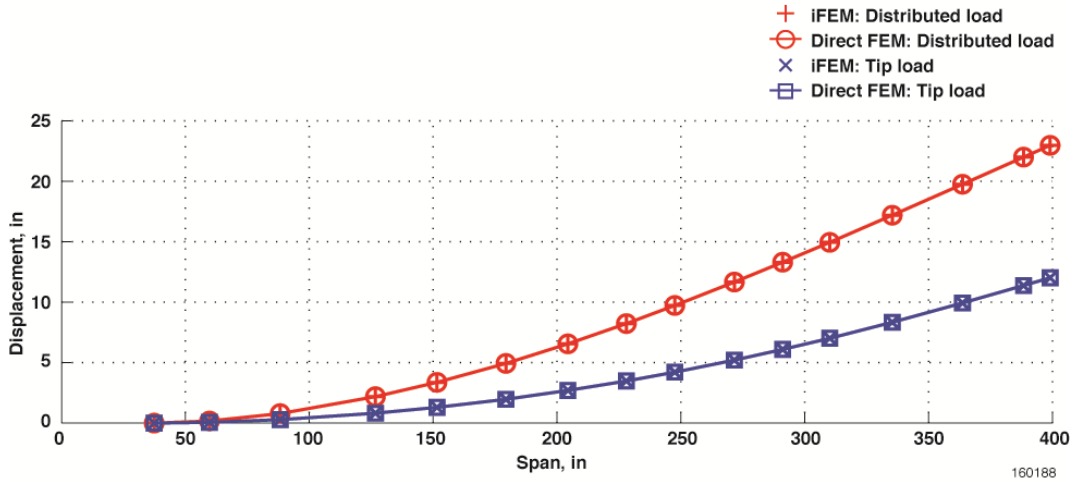
Figure 18. iFEM versus direct FEM displacements (sensor configuration = upper and lower surface).
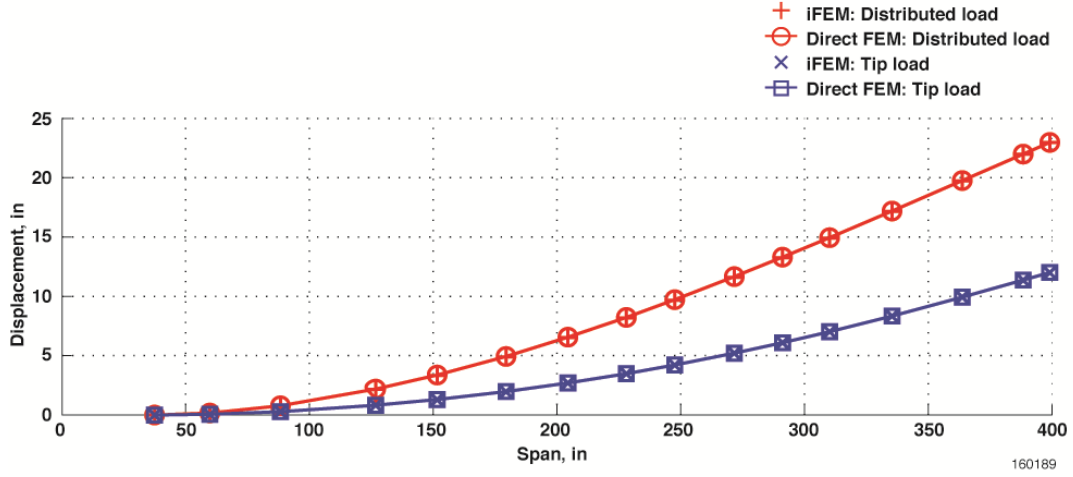
Figure 19. iFEM versus direct FEM displacements (sensor configuration = perimeter).
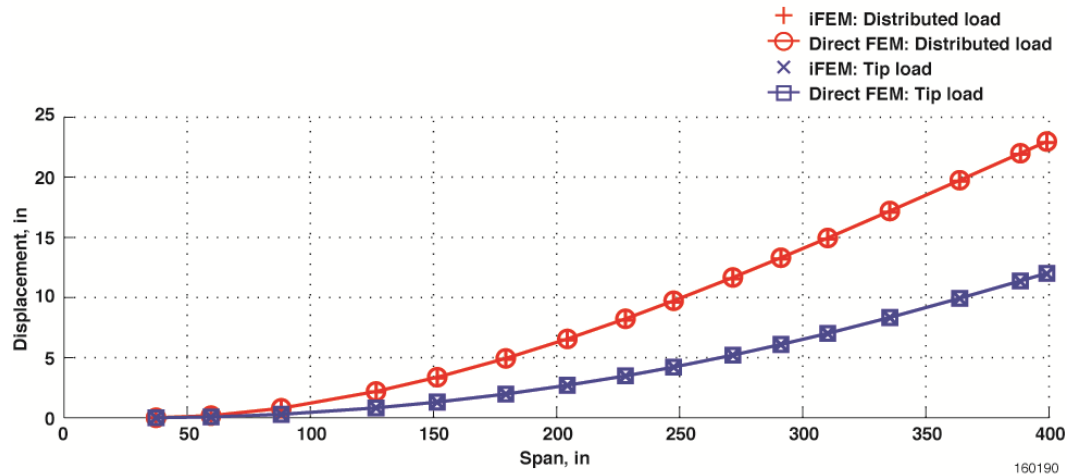
Figure 20. iFEM versus direct FEM displacements (sensor configuration = center rosette and axial strains).
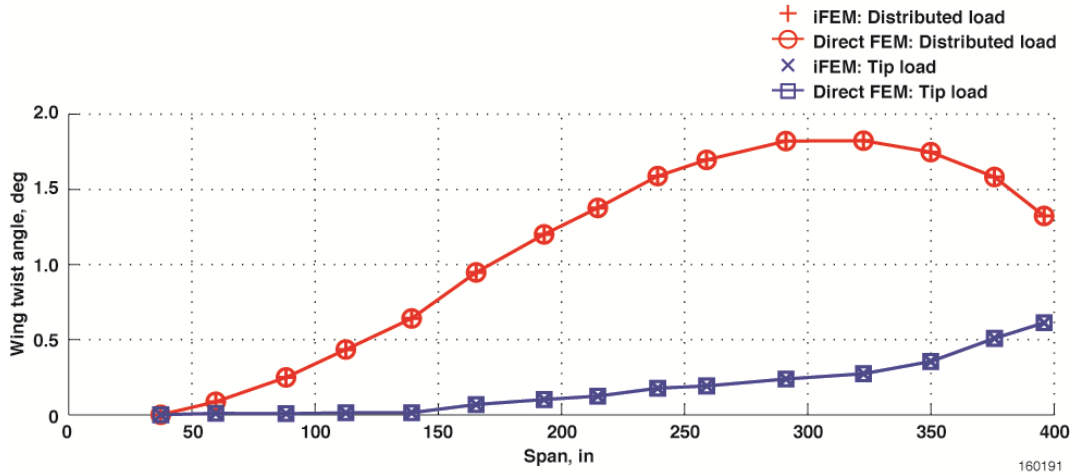
Figure 21. iFEM versus direct FEM twist angle (sensor configuration = full set).
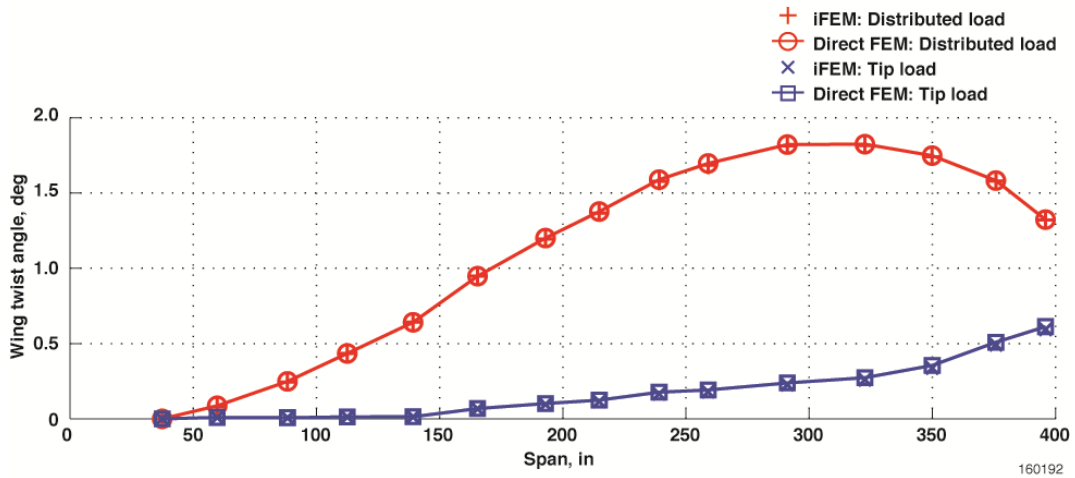
Figure 22. iFEM versus direct FEM twist angle (sensor configuration = upper and lower surface).
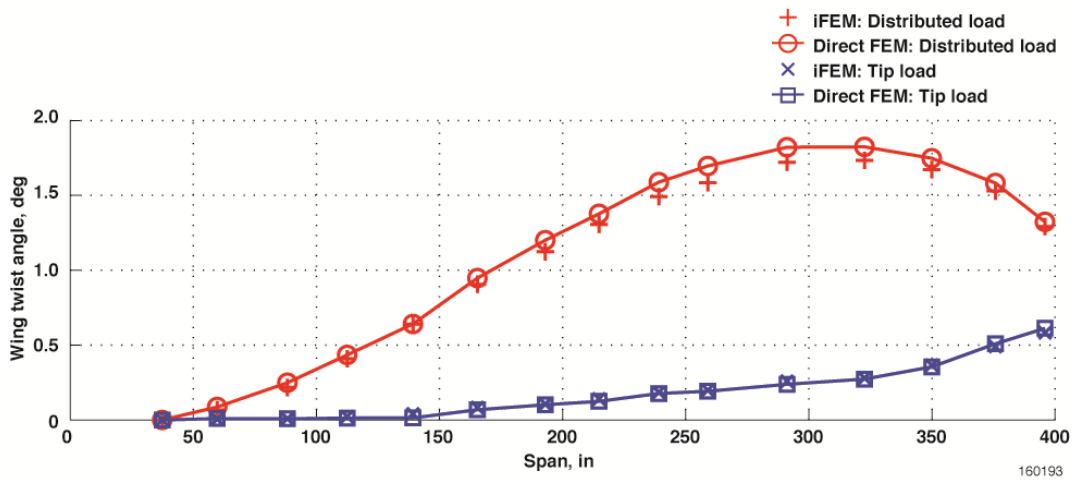
Figure 23. iFEM versus direct FEM twist angle (sensor configuration = perimeter).
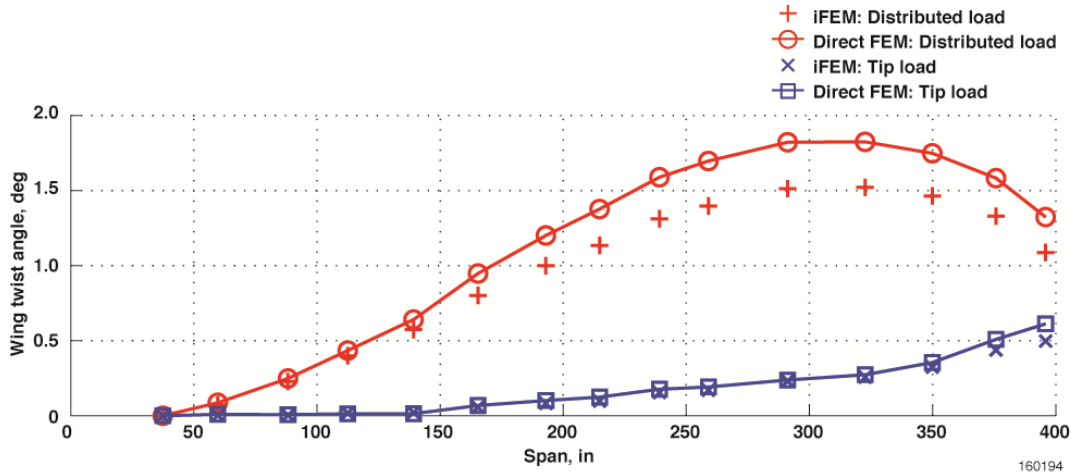
Figure 24. iFEM versus direct FEM twist angle (sensor configuration = center rosette and axial strains).
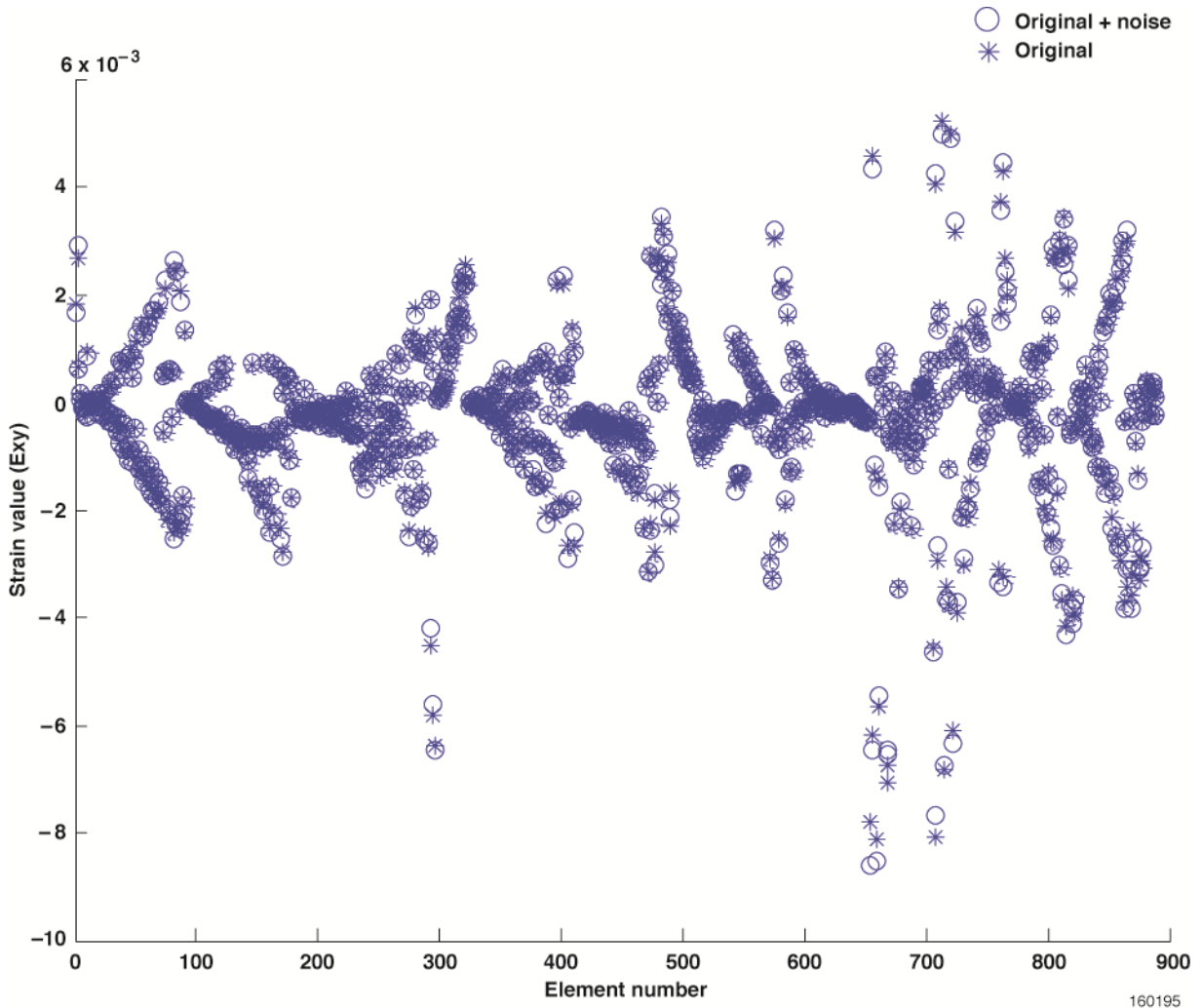
Figure 25. Strains with 10% noise: Original and original + noise strain (Exy) data.
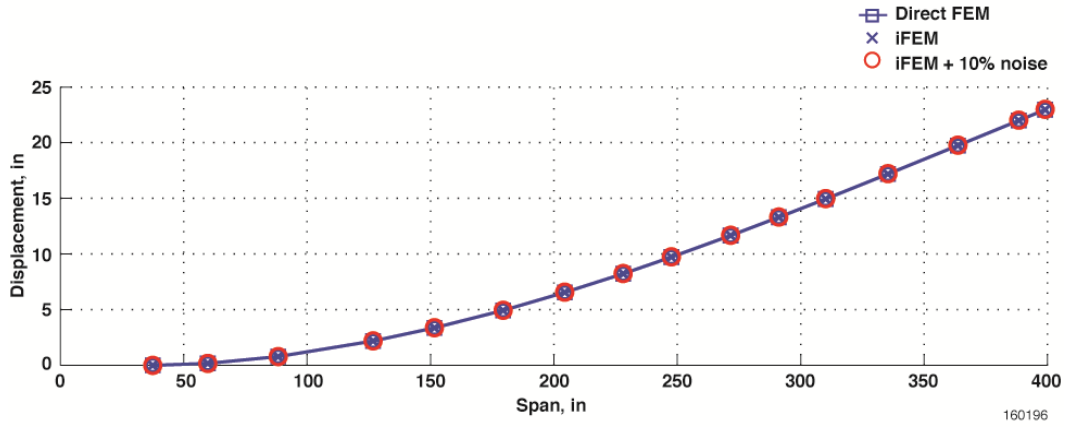
Figure 26. Effect of 10% noise on iFEM displacements (sensor configuration = full set).
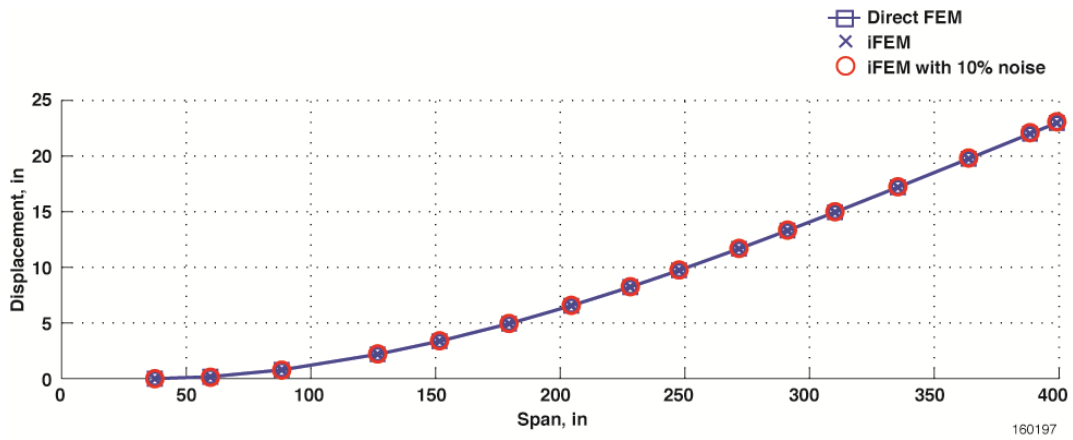
Figure 27. Effect of 10% noise on iFEM displacements (sensor configuration = upper and lower surface).
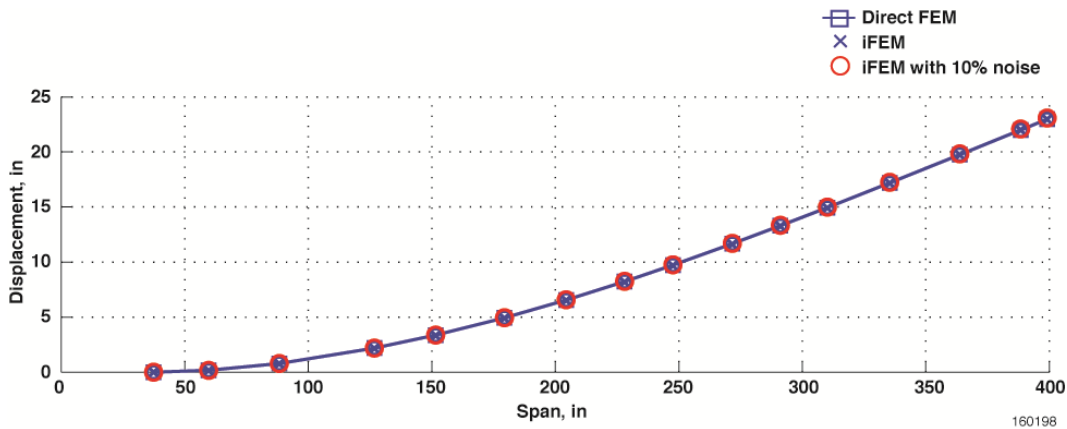

Figure 28. Effect of 10% noise on iFEM displacements (sensor configuration = perimeter).
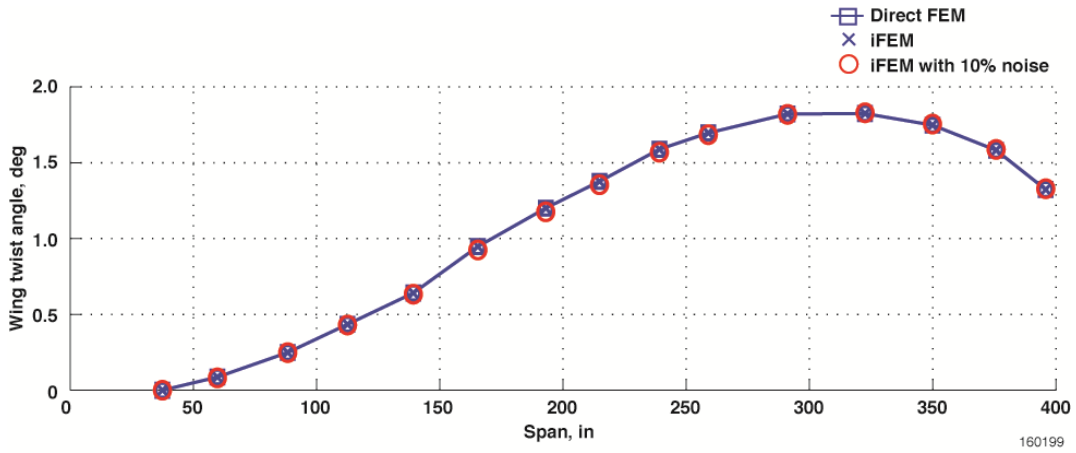
24

Figure 29. Effect of 10% noise on iFEM wing twist (sensor configuration = full set).
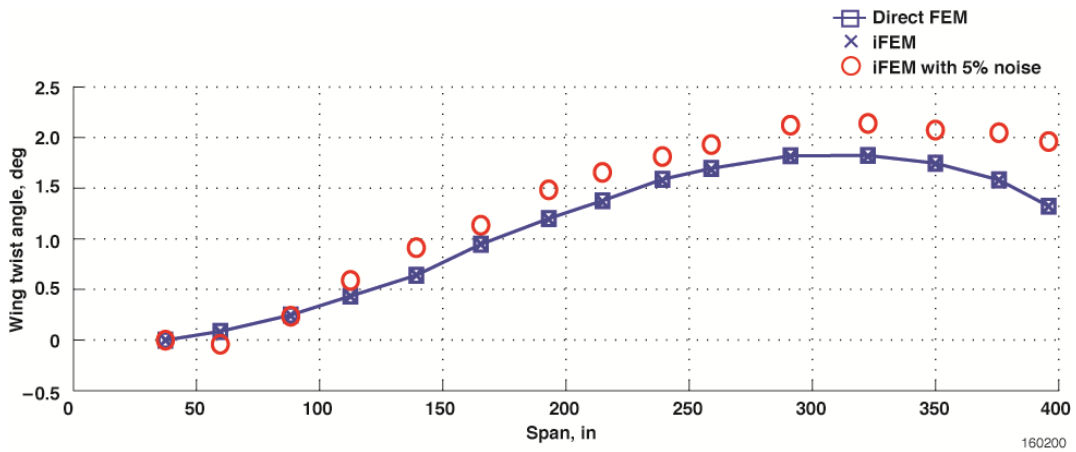

Figure 30. Effect of 5% noise on iFEM wing twist (sensor configuration = upper and lower surface).
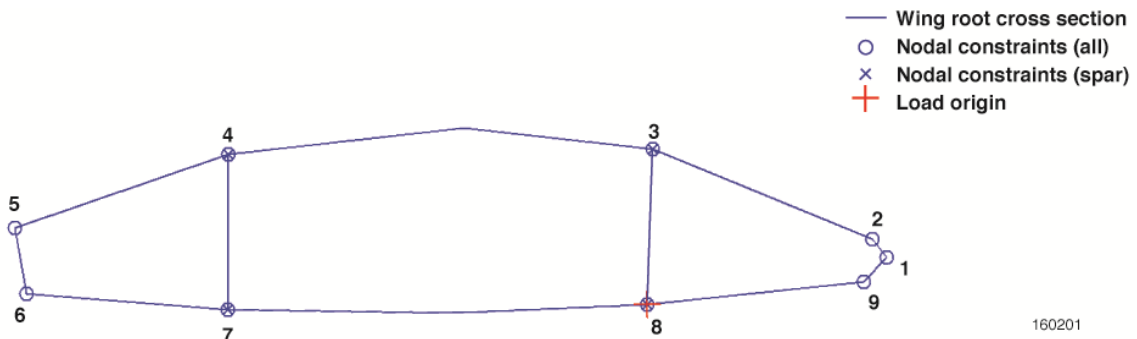

Figure 31. Locations for the load reactions at the wing root nodal constraints.
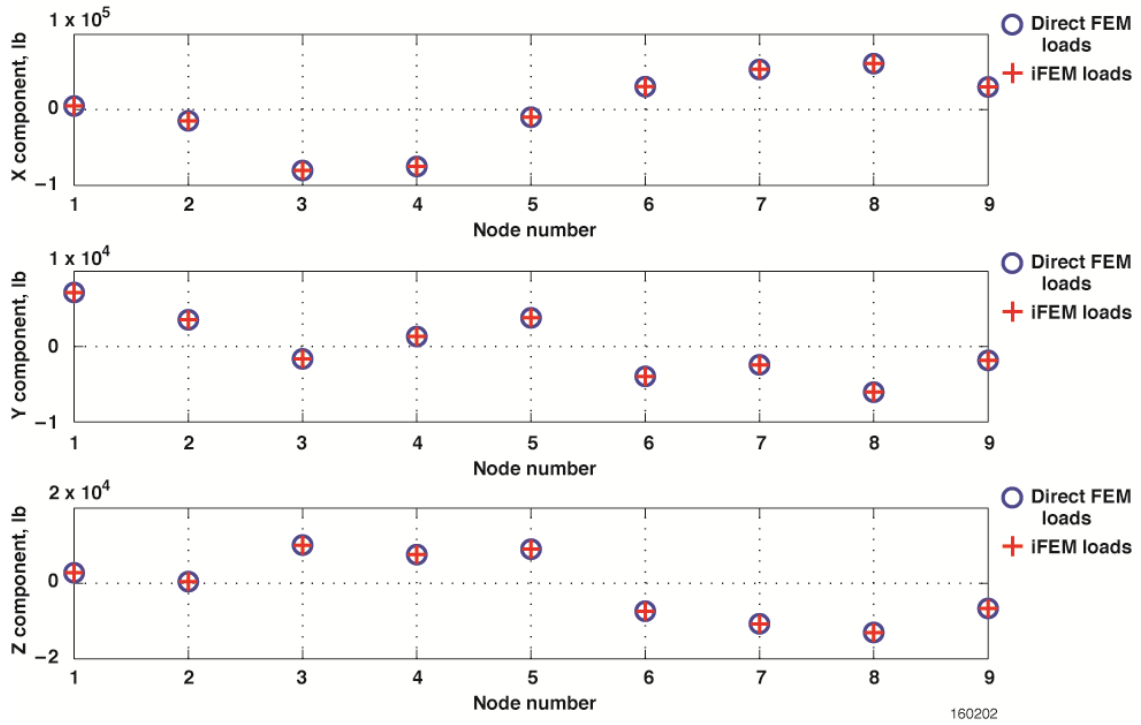
Figure 32. Reaction loads at the nodal constraints (sensor configuration = full set).
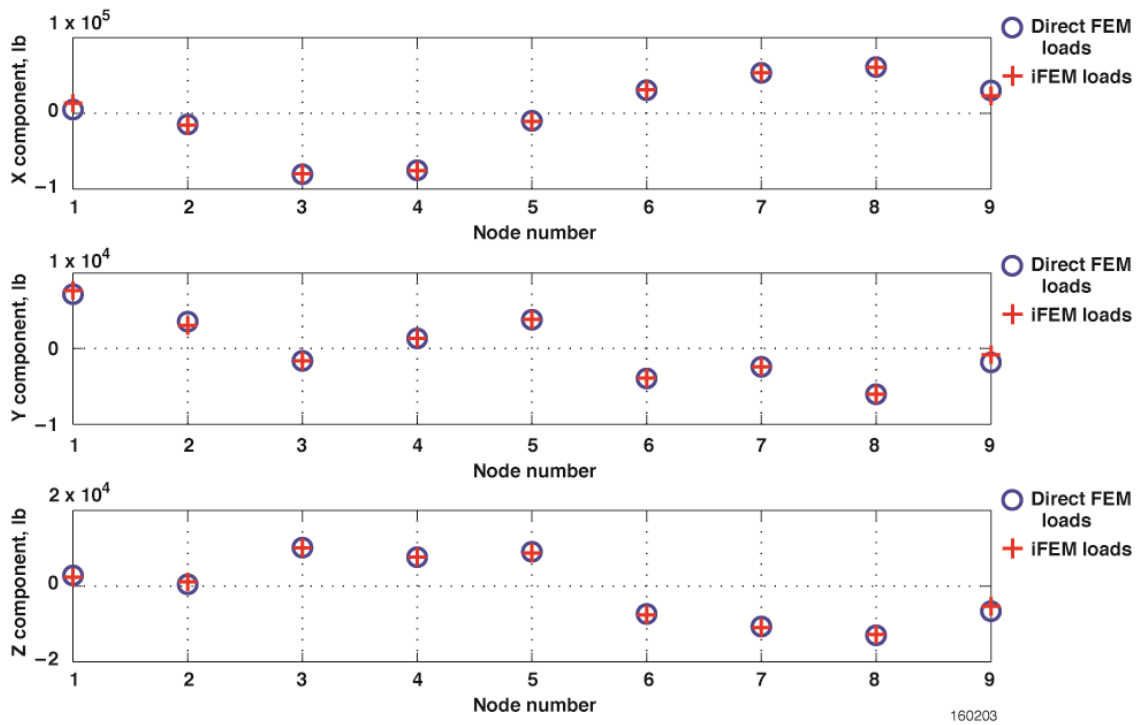

Figure 33. Reaction loads at the nodal constraints (sensor configuration = upper and lower surface).
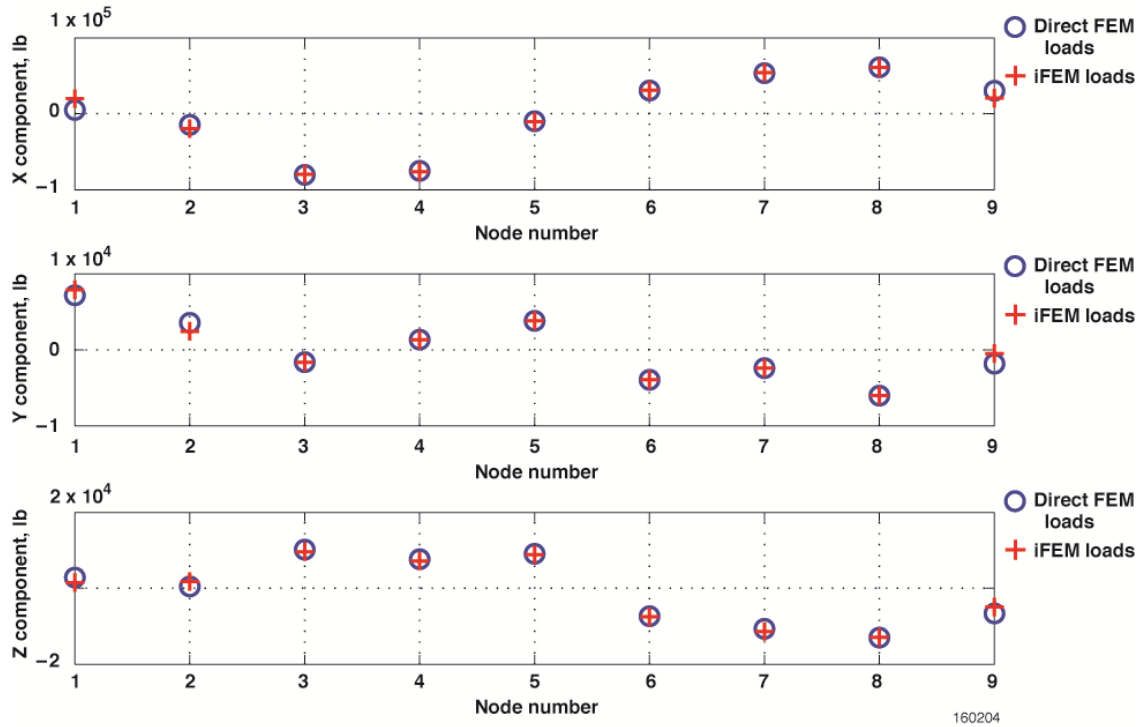
Figure 34. Reaction loads at the nodal constraints (sensor configuration = perimeter).

References

1. Jutte, Christine V., William L. Ko, Craig A. Stephens, John A. Bakalyar, W. Lance Richards, and Allen R. Parker, *Deformed Shape Calculation of a Full-Scale Wing Using Fiber Optic Strain Data from a Ground Loads Test*, NASA/TP-2011-215975, 2011.

2. Pak, Chan-gi, *Wing Shape Sensing from Measured Strain*, NASA/TM-2105-218358, 2015.

3. A.V. Tikhonov, V.Y. Arsenin, Solutions of ill-posed problems, Winston, Washington, DC, 1977.

4. Schnur. D. S., and Nicholas Zabaras, "Finite Element Solution of Two-Dimensional Inverse Elastic Problems using Spatial Smoothing," *International Journal for Numerical Methods in Engineering*, vol. 30, 1990, pp. 57-75.

5. Maniatty, Antoinette, Nicholas Zabaras, and Kim Stelson, "Finite Element Analysis of some Inverse Elasticity Problems," *Journal of Engineering Mechanics*, vol. 115, no. 6, 1989, pp. 1303-1317.

6. Maniatty, Antoinette M., and Nicholas J. Zabaras, "Investigation of Regularization Parameters and Error Estimating in Inverse Elasticity Problems," *International Journal for Numerical Methods in Engineering,* vol. 37, 1994, pp. 1039-1052.

7. Liu, Pei-Ling, and Hwei-Tser Lin, "Direct Identification of Non-Uniform Beams using Static Strains," *Int. J. Solids Structures,* vol. 33, no. 19, 1996, pp. 2775-2787.

8. Bogert, Philip B., Eric Haugse, and Ralph E. Gehrki, "Structural Shape Identification from Experimental Strains using a Modal Transformation Technique, AIAA-2003-1626, 2003.

9. Jones, R. T., D. G. Bellemore, T. A. Berkoff, J. S. Sirkis, M. A. Davis, M. A. Putnam, E. J. Friebele, and A. D. Kersey, "Determination of Cantilever Plate Shapes using Wavelength Division Multiplexed Fiber Bragg Grating Sensors and a Least-Squares Strain-Fitting Algorithm, *Smart Mater. Struct.,* vol. 7, 1998, pp. 178-188.

10. Shkarayev, S., R. Krashantisa, and A. Tessler, "An Inverse Interpolation Method utilizing In-Flight Strain Measurements for Determining Loads and Structural Response of Aerospace Vehicles," (available from ntrs.nasa.gov).

11. Shkarayev, S., A. Raman, and A. Tessler, "Computational and Experimental Validation enabling a Viable In-Flight Structural Health Monitoring Technology," *Proceedings of the First European Workshop on Structural Health Monitoring, 2002.*

12. Tesslcr, Alexandcr, Jan L. and Spanglcr, *A Variational Principle for Reconstruction of Elastic Deformations in Shear Deformable Plates and Shells*, NASA/TM-2003-212445, 2003.

13. Tesslcr, Alexandcr, and Jan L. Spanglcr, "Inverse FEM for Full-Field Reconstruction of Elastic Deformations in Shear Deformable Plates and Shells," 2004.

14. Tessler, Alexander, and Jan L. Spangler, "A Least-squares Variational Method for Full-Field Reconstruction of Elastic Deformations in Shear-Deformable Plates and Shells," *Comput. Methods Appl. Mech. Engrg.*, vol. 194, 2005, pp. 327-339, doi:10.1016/j.cma.2004.03.015.

15. Tessler, Alexander, *Structural Analysis Methods for Structural Health Management of Future Aerospace Vehicles*, NASA TM-2007-214871, 2007.

16. Vazquez, Sixto L., Alexander Tessler, Cuong C. Quach, Eric G. Cooper, Jeffrey Parks, and Jan L. Spangler, *Structural Health Monitoring Using High-Density Fiber Optic Strain Sensor and Inverse Finite Element Methods*, NASA/TM-2005-213761, 2005.

17. Gherlone, Marco, Priscilla Cerracchio, Massimiliano Mattone M., Marco Di Sciuva, and Alexander Tessler, "Shape Sensing of 3D Frame Structures using an Inverse Finite Element Method, *International Journal of Solids and Structures*, vol. 49, 2012, pp. 3100-3112, http://dx.doi.org/10.1016/j.ijsolstr.2012.06.009.

18. Kefal, Adnan, Erkan Oterkus, Alexander Tessler, and Jan L. Spangler, "A Quadrilateral Inverse-Shell Element with Drilling Degrees of Freedom for Shape Sensing and Structural Health Monitoring," Eng. Sci. Tech, Int. J. (2016), http://dx.doi.org/10.1016/j.jestch.2016.03.006.

19. Kefal, Adnan, Olgun Hizir, and Erkan Oterkus, "A Smart System to Determine Sensor Locations for Structural Health Monitoring of Ship Structures," Proceedings of the 9th International Workshop on Ship and Marine Hydrodynamics, 2015.

20. Kefal, Adnan, and Erkan Oterus, "Displacement and Stress Monitoring of a Panamax Containership using Inverse Finite Element Method," *Ocean Engineering*, vol. 119, 2016, pp. 16-29.

21. MSC Software Corporation, Newport Beach, California, www.mscsoftware.com [accessed November 22, 2016].

22. Jenkins, Jerald M., and V. Michael DeAngelis, *A Summary of Numerous Strain-Gage Load Calibrations on Aircraft Wings and Tails in a Technological Format*, NASA TM-4804, 1997.

23. Skopinski, T. H, William S. Aiken, Jr., and Wilbur B. Huston, *Calibration of Strain-Gage Installations in Aircraft Structures for the Measurement of Flight Loads*, NACA Report 1178, 1954.